Cite This as Applied Catalysis B: Environmental**;** Volume 253, 15, 2019, Pages 401-418

Theoretical and experimental investigation of visible light responsive $AgBiS_2$-TiO_2 heterojunctions for enhanced photocatalytic applications

Priyanka Ganguly[1,2], Snehamol Mathew[1,2], Laura Clarizia[3], Syam Kumar R[4], A. Akande[4], Steven Hinder[5], Ailish Breen[1,2], Suresh C. Pillai[1,2*]

[1]Nanotechnology and Bio-engineering Research Group, Department of Environmental Science, Institute of Technology Sligo, Sligo, Ireland.

[2]Centre for Precision Engineering, Materials and Manufacturing Research (PEM), Institute of Technology Sligo, Sligo, Ireland.

[3]Dipartimento di Ingegneria Chimica, dei Materiali e della Produzione Industriale, Università di Napoli Federico II, p. le V. Tecchio 80, 80125 Napoli, Italia.

[4]Mathematical Modelling Research Group, Department of Health and Nutritional Sciences, Institute of Technology Sligo, Sligo, Ireland.

[5]The Surface Analysis Laboratory, Faculty of Engineering and Physical Sciences, University of Surrey, Guildford, Surrey, GU2 7XH, United Kingdom

**Corresponding authors E-mail address: pillai.suresh@itsligo.ie*

ABSTRACT:

The formation of heterostructure nanocomposite has been demonstrated to be an effective route to enhance the photocatalytic efficiency. Ternary chalcogenides (TC) with remarkable visible light absorption, are identified as an ideal candidate to form heterostructure with classical semiconductors such as TiO_2. In the current investigation, novel heterojunctions of the $AgBiS_2$-TiO_2 composite were synthesised using a solvothermal technique. Computational analysis was utilised to study the electronic and optical properties of the pristine parent samples. The XRD results show the formation of the cubic phase of $AgBiS_2$ and TiO_2 is in tetragonal phase. The XPS and the TEM results illustrate the heterostructure formation. The UV-DRS pattern for all the composites shows enhanced visible light absorption due to the coupling of TC. The band gaps of the composites were decreased with increased doping levels. These materials were further studied for their photocatalytic efficiency, by photocatalytic degradation of Doxycycline, photocatalytic hydrogen generation and photocatalytic antimicrobial disinfection. The composite samples illustrated more than 95% degradation results within 180 minutes and showed about 3 log reductions of bacterial strains (*E. coli* and *S. aureus*) within 30 minutes of irradiation. The hydrogen production results were interesting as the $AgBiS_2$

based composites illustrated a 1000-fold enhanced output. The enhanced photocatalytic activity is attributed to the decreased rate of recombination of the photogenerated excitons, as validated in the PL measurements. The scavenging experiments along with the theoretical analysis are used to define a plausible photocatalytic mechanism.

Keywords; Ternary chalcogenides; Photocatalysis; Water splitting; Antimicrobial disinfection; Degradation.

1. Introduction

Environmental pollution and the ever increasing demand for energy has resulted in the search for efficient sustainable technologies.[1, 2] Hydrogen is identified as the fuel for the forthcoming decades, while at present steam reforming is the major industrial route for synthesising H_2 gas.[3-6] Alongwith energy, the need for safe water for the rising earth population has turned to be a foremost crisis.[7, 8] The existing water treatment plants employ conventional methods such as sedimentation, flocculation, adsorption and even the use of membrane technologies for secondary treatment plants.[9, 10] This often results in release of additional chemicals into the ecosystem, moreover, the threat of the presence of industrial effluents and pharmaceutical waste has reached to its epitome.[11] Therefore, effective renewable sustainable technologies is of paramount importance. [7, 8] Solar energy conversion utilising semiconductor photocatalysis obtained after appropriate band structure alteration is one of the vital strength for green energy and environmental remediation. In order to attain appreciable photocatalytic efficiency, the factors to be considered in design and development are (a) improving the visible light absorption (b) promoting the separation of photogenerated excitons and (c) promotion of these excitons transfer to the surface, where the reaction occur.[12, 13] As a vital approach, to improve the visible light absorption can be achieved by utilising novel semiconductor materials such as ternary chalcogenide (TC) compounds.[14, 15] TC are an interesting class of materials, these multicomponent chalcogenides have garnered enough attention in recent years for their effective electro-optical properties, and used for potential applications in biomedical imaging, photovoltaic devices, LEDs, phase change memory devices.[16-18] Among them, the family of I-V-VI has gained significant interest because of their wide band gap and high visible light absorption.

$AgBiS_2$ (I-V-VI), a ternary semiconductor material is a very common mineral sulfbismuthide in nature (matildite). It exists in two phases, namely, the low-temperature phase β-$AgBiS_2$ with a hexagonal structure and the elevated temperature phase α-$AgBiS_2$ with a cubic structure. The phase transition temperature is 195 °C.[19] The nanocrystals of $AgBiS_2$ are reportedly synthesised through various methods such as solid-state reaction, solid solution technique, flux technique, microwave-assisted method, hydro/solvothermal procedure, polyol route and sonochemical techniques.[20-25] The narrow band gap and the high visible light absorption benefits in different functional applications. However, these semiconductor exhibits low quantum efficiency and strong light etching which restricts its large-scale applications.[26, 27]

In order to promote the separation of photogenerated excitons, the visible light absorption, alone cannot promote high photocatalytic efficiency, thereby there requires possible structural or morphological manipulation.[28] Hence, heterostructure formation with other classical semiconductors such as TiO_2 can possibly aid in delaying the excitons recombination.[27] TiO_2 due to its high structural and photostability along with facile synthesis process makes it an ideal photocatalytic candidate.[29] However, the poor visible light absorption and wide band gap decrease their catalytic efficiency.[30, 31] Therefore, the formation of heterostructure composite with $AgBiS_2$ could potentially increase the photocatalytic efficiency by decreasing the composite bandgap and by enhancing the charge transfer. Finally, the challenge to overcome the lack of exciton population on the photocatalytic surfaces could be possibly evaded by structural manipulations.[32] The staggered band alignment of a possible heterostructure would promote the delaying of the photogenerated electron-hole pair recombination, which effectively enhances the interfacial charge transfer.[29, 33]

$AgBiS_2$-TiO_2 heterostructure for solar cell application has been reported. Zhou *et al.* reportedly synthesised $AgBiS_2$ quantum dots (QDs) and assembled onto TiO_2 nanorods film for QD-sensitized solar cell (QDSSC).[34] However, there exists a definite paucity in correlating the theoretical concepts on the structural details of the semiconductor materials with the experimental process. There are no reports of these novel composites with a complete understanding and evaluation of their photocatalytic behaviour by various functional applications.

Therefore, in this present study, a solvothermal technique was utilised to synthesize $AgBiS_2$-TiO_2 composite. Stable and visible light improved effective heterojunctions of $AgBiS_2$- TiO_2 at different weight percent loading were developed (0.5, 1, 2 and 5 wt%) and further evaluated for photocatalytic degradation of Doxycycline, photocatalytic hydrogen generation and photocatalytic antimicrobial disinfection. Computational analysis of the structural, electronic and optical properties of the pristine parent samples (TiO_2 and $AgBiS_2$) were studied. The as prepared composites illustrated homogeneous distribution as observed in TEM images and showed composite formation through Raman and XPS analysis. The composites of $AgBiS_2$-TiO_2 displayed 1000-fold enhanced photocatalytic H_2 production compared to $AgBiS_2$ and TiO_2 samples. Similar results were also observed for bacterial disinfection activity, where the $AgBiS_2$-TiO_2 exhibited better results compared to its pristine counterparts. Furthermore, the degradation results were also impressive as the composites exhibited more than 95% activity within 180 mins of visible light irradiation. A plausible photocatalytic mechanism based on the computational results, PL measurements and the scavenger experiments have been proposed.

2. Materials and method

2.1. Chemicals and Reagents

All the materials used were of analytical grade. Silver nitrate ($AgNO_3$), Bismuth(III) nitrate pentahydrate ($Bi(NO_3)_3 \cdot 5H_2O$), Thiourea (CH_4N_2S), Titanium(IV)isopropoxide ($C_{12}H_{24}O_4Ti$), Ethanolamine ($NH_2CH_2CH_2OH$), Benzoquinone ($C_6H_4O_2$), Isopropanol ($(CH_3)_2CHOH$), Ethanol (CH_3CH_2OH), Methanol (CH_3OH), Doxycycline hyclate ($C_{22}H_{24}N_2O_8 \cdot HCl \cdot 0.5H_2O \cdot 0.5C_2H_6O$) were purchased from Sigma-Aldrich. Triethanolamine ($C_6H_{15}NO_3$) was bought from PanReac AppliChem ITW reagents. Distilled water was used in all experiments. For Antimicrobial studies, strains of *Staphylococcus aureus* (ATCC-25923) and *Escherichia coli* (ATCC-25922) were purchased from LGC Standards. Agar nutrient, Nutrient broth No.2, and 90 mm Petri dishes were bought from Cruinn Diagnostics. Phosphate-buffered saline tablets were supplied from VWR.

2.2. Synthesis

TiO_2 was synthesized using a sol-gel method. The required amount of titanium isopropoxide (TTIP) was stirred in isopropanol for 15 min. The water was added dropwise to the previous solution under vigorous stirring. The ratio of water and isopropanol was kept constant (1:1) and the resultant solution was kept for gelation for 2 hrs. Furthermore, the gel was dried in an oven at 100 °C for 12 hrs followed by calcination at 500 °C, at a ramp rate of 10 °C/min for 2 hrs.

The $AgBiS_2$-TiO_2 heterostructure composites were prepared by a simple solvothermal technique. In this process, $AgNO_3$, $Bi(NO_3)_3.5H_2O$ and thiourea at a ratio of 1:1:2 was weighed and mixed in 30 mL of ethanolamine under vigorous stirring. The stirring was continued for one hour and the as-synthesised TiO_2 was added into the above solution. This mixture was further ultra-sonicated for another 30 mins, such that the final composites result in the ratio of 0.5/1/2 & 5 wt % $AgBiS_2$ with remaining TiO_2. The above mixture solution was placed in a 50 mL steel Teflon vessel (from Parr instruments) and heated up to 180 °C for 24 h for $AgBiS_2$-TiO_2 composites. The resultant solid product was washed multiple times with water and ethanol to remove the solvent residue and later dried overnight at 60 °C. The dried powder obtained was used for further characterisation and applications. The same protocol was used for synthesising parent sample ($AgBiS_2$) without adding TiO_2.

2.3. DFT/ Computational calculations

Density Functional Theory (DFT) as implemented in the all electron code, Fritz Haber Institute *Ab Initio* Molecular Simulations (FHI-AIMS) package was used to obtain the structural, electronic and dielectric properties of TiO_2 and $AgBiS_2$.[35] The Perdew-Burke-Ernzerhof (PBE) generalised gradient approximation (GGA) was used in all the calculations.[36] The basis sets used in all the calculations were the ‘tight’ high accuracy all-electron numerical atomic orbitals (NAO) basis sets provided by the FHI-AIMS by default. To account for the long range van der Waals interactions, the Tkatchenko and Scheffler (TS) correction scheme was also applied in the calculations involving structural relaxation.[37] Broyden-Fletcher-Goldfarb-Shanno (BFGS) algorithm was used to relax the atomic positions and lattice vectors of the structures under consideration.[38] The reciprocal space integration was performed over the 8x8x8 grid. The convergence criteria used for the structural relaxation includes the eigenvalues, total energies and forces which were set to 10^{-3}, 10^{-4} eV and 10^{-3} eV/Å respectively. Furthermore, the calculation of the electronic and dielectric properties was carried out by including the effect of Spin-Orbit Coupling (SOC).[39] The initial geometries of TiO_2 and $AgBiS_2$ were obtained from the Materials Project Library.[40]

2.4. Characterisations

X-ray diffraction (XRD) was used to analyse the crystallinity and phase of the prepared samples. In Siemens D500 X-ray powder diffractometer, the diffractograms were produced using Cu Kα radiation (λ= 0.15418 nm) at 40 kV and 30 mA. The diffraction was examined in the range of 10°- 80° with the constant scan rate at 0.2°/s.

The phase transformation was analysed using Raman spectroscopy (Horiba Jobin Yvan LabRAM HR 800) with a grating of 300 gr/mm. A solid-state diode laser (660 nm) standard bandwidth version with double edge filter upgrade was used with the acquisition time of 3 seconds.

The bonding interactions and oxidation state of elements were studied with the help of X-ray photoelectron spectroscopy. XPS analyses were performed on a ThermoFisher Scientific Instruments (East Grinstead, UK) K-Alpha+ spectrometer. XPS spectra were acquired using a monochromated Al Kα X-ray source (hν = 1486.6 eV). An X-ray spot of ~400 μm radius was employed. Survey spectra were acquired employing a Pass Energy of 200 eV. High resolution, core level spectra for all elements were acquired with a Pass Energy of 50 eV. All spectra were charge referenced against the C1s peak at 285 eV to correct for charging effects during acquisition. Quantitative surface chemical analyses were calculated from the high resolution, core level spectra following the removal of a non-linear (Shirley) background. The manufacturers Avantage software was used which incorporates the appropriate sensitivity factors and corrects for the electron energy analyser transmission function.

The characteristic absorptions of the as prepared samples were measured using a Perkin- Elmer Lambda 35 UV-Vis Spectrophotometer equipped with reflectance measuring attachment. Barium sulphate ($BaSO_4$) was used as a reference and slit width was set to 1 nm. Band gaps were calculated using both Kubelka-Munk function and Tauc equation. Where Kubelka-Munk function F(R);

$$F(R) = \frac{(1-R)^2}{2R} \text{ (Equation 1)}$$

Where R is the absolute reflectance of the sample.

And Tauc equation is;

$$(h\vartheta\alpha)^{1/n} = A(E - E_g) \text{ (Equation 2)}$$

Where A = Constant depending on the properties of the material.

E = Energy of the incident photon.

E_g = Band gap of the material.

h = Planck's Constant.

ν = Frequency of the incident photon.

n = Constant that depends on the type of electronic transition, where;

n= ½ for permitted direct transition

n = 3/2 for prohibited direct transition

n = 2 for permitted indirect transition

n = 3 for prohibited indirect transition.

The obtained diffused reflectance of the sample is converted to Kubelka-Munk function as F(R) is proportional to the absorption coefficient. The α in the Tauc equation is substituted with F(R). Hence, the equation becomes; [41]

$$(h\vartheta F(R))^{1/n} = A(E - E_g) \text{ (Equation 3)}$$

The morphology and microstructure of the samples were imaged using a JEOL 2100 Transmission Electron Microscope (TEM) at an accelerating voltage of 200 kV with Lanthanum Hexaboride emission source.

Photoluminescence (PL) spectra were obtained using a Perkin-Elmer LS55B luminescence spectrometer with a pulsed Xenon discharge lamp. The measurements were recorded using an excitation wavelength set at 320 nm and emission measured from 330 nm to 800 nm.

The photocatalytic degradation of Doxycycline and microbial disinfection experiments were performed inside a weathering and corrosion photo-reactor from Q-Labs (Q-sun Xe-1-S) using a Xenon lamp source (500 W), equipped with a window glass filter. The irradiation intensity is fixed at 1.1 W/m^2 and the chamber temperature was maintained at 38°C.

2.5. Photocatalytic degradation reaction

The photocatalytic activities of as-synthesized $AgBiS_2$-TiO_2 composites were evaluated by photodegradation of doxycycline (DC) under visible light illumination using a photochamber unit. In a typical photocatalytic experiment, 0.08 g of photocatalyst was dispersed in 80 ml of aqueous DC (10^{-5} M) solution. Prior to irradiation, the resultant suspension was magnetically stirred for 60 min in dark to attain absorption-desorption equilibrium. After every 15 minutes of illumination period, aliquots were withdrawn to measure the concentration of DC with a UV-Vis spectrophotometer in the spectral range of 200 to 800 nm. Doxycycline exhibits strong characteristic absorption peaks at 278 and 357 nm. The reduction in intensity of the peak at 357 nm is monitored with time for the degradation profiles. For comparative assessment, photocatalytic degradation of pristine parent samples (TiO_2 and $AgBiS_2$) were also carried out under identical conditions. After every experiment, the photocatalysts were centrifuged, washed, dried, and reused to evaluate the recyclability of the samples. The degradation ratios were calculated by the equation;

$$\%DC\ degraded = \left(\frac{C_0 - C_t}{C_0}\right) \times 100 \text{ (Equation 4)}$$

Where C_0 (mg L^{-1}) and C_t (mg L^{-1}) correspond to the DC concentration at the initial and after contact time t (min) respectively.

Scavenging Experiment

In order to evaluate the reactive oxygen species generated in the reaction system, different scavenger tests were performed. 10 mM isopropanol [a quencher of hydroxyl radicals (OH^{-})], 6 mM $AgNO_3$ (a quencher of electron), 6 mM benzoquinone [a quencher of superoxide radicals ($O_2^{\cdot-}$)] and 10 mM triethanolamine (a quencher of holes) are added respectively in 4 different photocatalytic systems, with 0.08 g of photocatalyst dispersed in 80 ml of aqueous DC (10^{-5} M) solution. These systems were further subjected to light irradiation for 180 mins, prior to the illumination they were kept for 60 min in dark to achieve the adsorption-desorption equilibrium. Aliquots after every 15 min were taken and estimated for DC concentration as explained above for the photocatalytic experiments.

2.6. Photocatalytic hydrogen generation

Photocatalytic runs have been carried out in an annular glass batch reactor (V =300 mL) covered with a layer of aluminium foil. On the top of the reactor, an inlet has allowed to feed reactants and nitrogen gas, and an outlet has been used to collect liquid and gaseous samples at different reaction times.

The reactor has been endowed with a high-pressure mercury vapour lamp by Helios Italquartz (power input: 125 W) and a high-pressure sodium vapour lamp by (power input: 150 W), both of which are from Helios Italquartz. The reactor has been cooled at 25 °C during each run by means of a thermostatic bath (Falc GTR 90).

The pH of the solution has been monitored by means of an Orion 420Aþ pH-meter (Thermo).

In order to avoid the undesired reaction of dissolved oxygen with photogenerated electrons, before starting the photocatalytic runs, a nitrogen stream has been bubbled into the solution for 30 minutes for removing atmospheric oxygen. Moreover, throughout the experiments, nitrogen has been continuously fed at a flow rate (Q_{N_2}) of 0.3 L/min to prevent any entrance of air into the reactor. For each run, fixed amounts of catalyst and methanol have been added to 300 mL of aqueous solution; the resulting suspension has been fed into the batch reactor under magnetic stirring.

The liquid samples, collected at different reaction times, have been quickly filtered on regenerated cellulose filters (pore diameter 0.20 μm, Scharlau) and the filtrate has been used to measure pH. The gaseous samples have been recovered from the reactor outlet in Tedlar gas sampling bags and then used to evaluate hydrogen concentration.

Hydrogen concentration has been measured by a gas-chromatograph (Agilent 7820A) equipped with a HP–PLOT Molesieve 5A column (Agilent) and a TCD detector using argon as carrier gas.

During the experiments, the radiation emerging from the reactor has been measured on the external walls of the reactor by means of proper radiometers (not shown in Figure 1) in the wavelength ranges of 315-400 nm and 400-1100 nm.

In the same experimental runs, at a fixed reaction time (60 minutes) a solution of sodium nitrite (1 M) has been introduced inside the cooling jacket for controlling the temperature (25°C) and for cutting-off UVA radiation emitted by the lamp ($\lambda < 400$ nm).

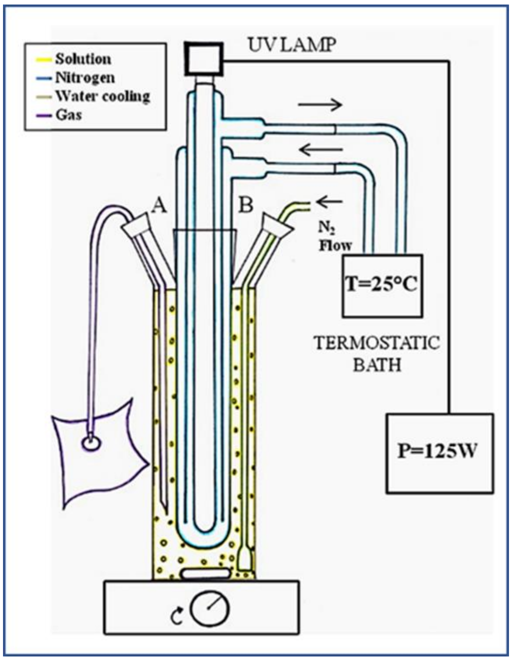

Figure 1. Schematic illustration of the photocatalytic reactor (A) outlet and (B) inlet.

2.7. Photocatalytic antimicrobial activity

All the glassware used for the photocatalytic disinfection experiments were autoclaved prior to their use. Two strains of bacteria, one gram-negative (*E. coli*) and the other gram-positive (*S. aureus*) were utilised to evaluate the light induced disinfection ability of the as prepared $AgBiS_2$-TiO_2 composites and further compared with their pristine parent samples (TiO_2, and

$AgBiS_2$). 25 g of nutrient broth No.2 (10 g peptone, 5.0 g NaCl, 10 g beef extract) was dissolved in 1 L of distilled water to make the nutrient broth culture medium, which is further sterilized at 121 °C using an autoclave. 28 g nutrient agar (5 g peptone, 8.0 g NaCl, 3.0 g beef extract, Agar No.2) was dissolved in 1L of distilled water and further autoclaved at 121 °C for 15 mins and later poured into 90 mm agar plates. The strains were inoculated in 20 ml of nutrient broth and incubated for 24 h at 37 °C. A certain volume of the grownup culture was transferred to the cylindrical glass vessel to make the working solution of 10^4 CFU/mL (colony forming unit/ml). The reaction suspension was placed inside the photo test chamber for visible light illumination. The photocatalyst concentration was fixed at 1 g/L and illuminated for an overall 3 h. Additionally, aliquots of 1 mL were removed out from the reaction suspension at a regular time interim of 15 mins. In order to achieve a countable CFU the bacterial solution was diluted once in 9 ml PBS solution and later 100 μL of the diluted solution was plated. Lastly, the plates were incubated at 37 °C for 24 h. The colonies developed on the agar plates were calculated and recorded as CFU/mL. Control experiments were also performed in the absence of the photocatalyst. The same set of samples were tested simultaneously under dark conditions to understand the importance of light in the experiment. The antimicrobial efficiency was calculated using 2 methods; i) log reduction and ii) N/N_0% vs time.[42, 43] Where,

$$\text{log reduction} = log_{10}\frac{(A)}{(B)} \Rightarrow \log_{10}(A) - \log_{10}(B) \qquad \text{(Equation 5)}$$

Where A = initial number of viable microorganisms

B = number of viable microorganisms at any time “t”.

Now,

$\log_{10}(A) \rightarrow N_0$

$\log_{10}(B) \rightarrow N$ for any time “t”.

3. Results

3.1. Computational analysis

The crystal structures of TiO_2 and $AgBiS_2$ have been fully relaxed. TiO_2 crystallises into the tetragonal crystal structure and shown in Figure 2. Ti and O are connected to each other in octahedral molecular geometry and the octahedra are connected to each other by the alternate edge and corner sharing. The lattice parameters of the relaxed structure of tetragonal TiO_2 crystal are a = b = 10.1621 Å, c = 2.9605 Å and α = β = γ = 90˚.

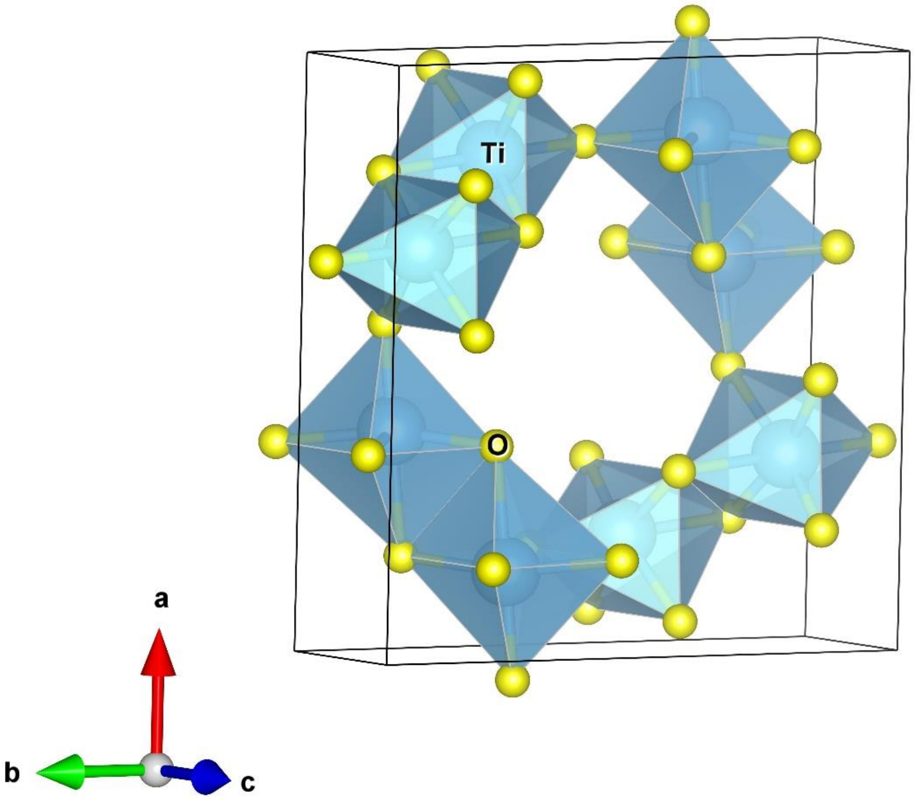

Figure 2. (Colour Online) Optimised structure of TiO_2. Fully relaxed tetragonal crystal structure of TiO_2. Colour code: blue = Ti and yellow = O.

$AgBiS_2$ is layered and found to be stable in trigonal crystal structure and is given in Figure 3. BiS_6 octahedra are separated by AgS_6 tetrahedra in its unit cell. In the relaxed structure, the lattice parameters of trigonal $AgBiS_2$ are a = b = 4.0817 Å, c = 19.3362 Å, α = β = 90˚ and γ = 120˚.

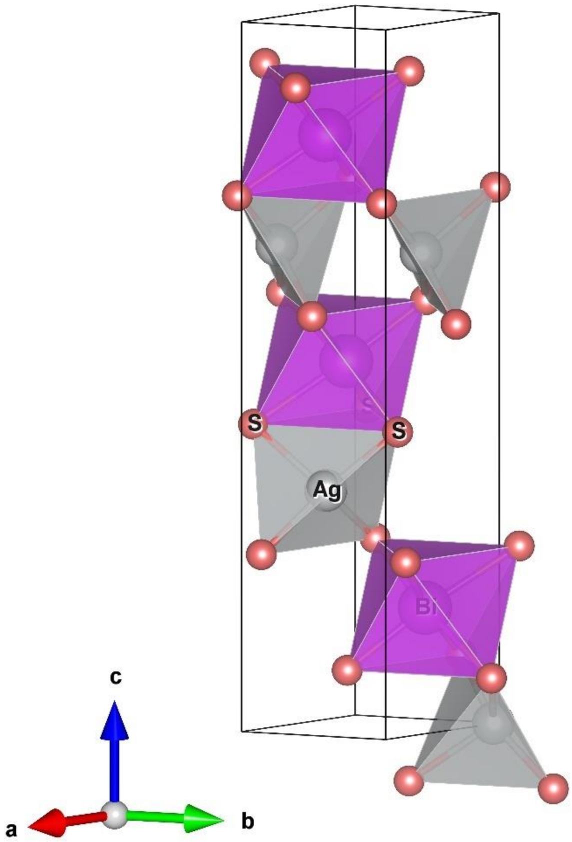

Figure 3. (Colour Online) Optimised structure of Silver Bismuth Sulphide ($AgBiS_2$). Fully relaxed trigonal structure of $AgBiS_2$. Colour code: grey = Ag, light pink = Bi, red = S.

The band structure and the partial density of state (PDOS) of TiO_2 are shown in Figure 4. The system has a computed indirect band gap of ~ 2.7 eV. The valence band maxima (VBM) lies between Z and P k-points and the conduction band minima (CBM) lie between the Γ and X k-points in the reciprocal space. The upper valence band (UVB) is dominated by O p-states and the lower conduction band (LCB) is dominated by Ti d-states. There is the presence of Ti p-states also near the UVB.

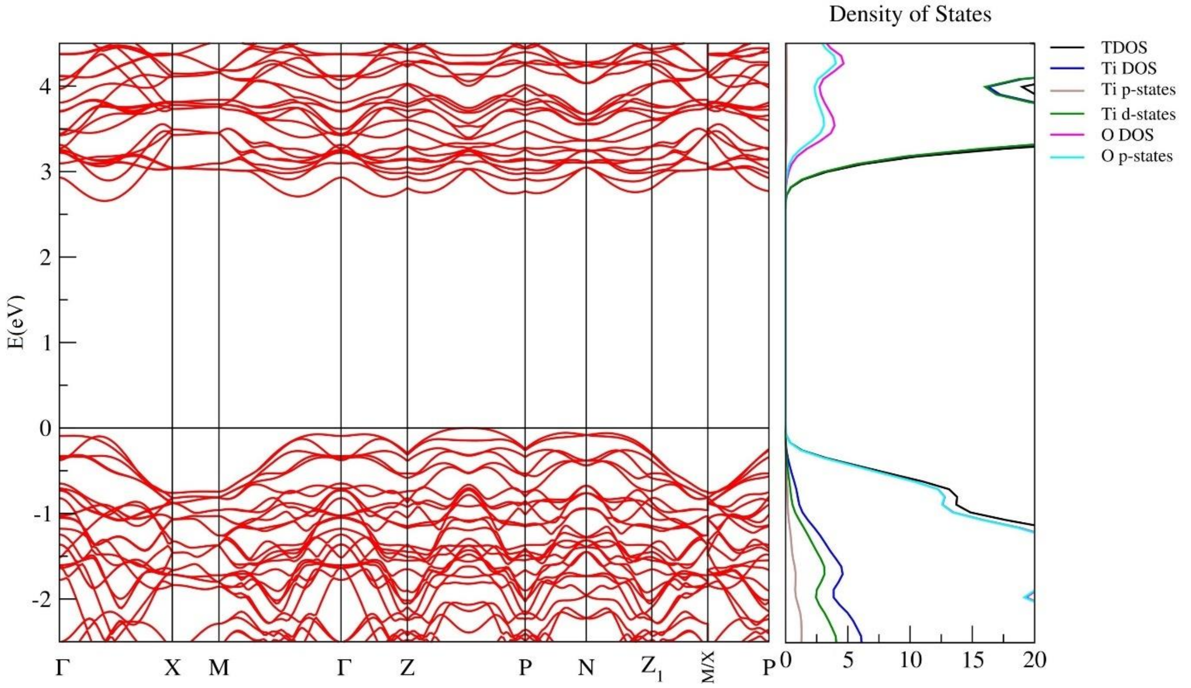

Figure 4. Optimised electronic structure of TiO_2. Calculated band structure for TiO_2. The valence band top is aligned at 0 eV (horizontal line) with the corresponding PDOS.

Figure 5 shows the computed band structure and the PDOS of $AgBiS_2$. The system has an indirect bandgap of ~0.7 eV. The VBM lies between the H and A k-points and the CBM lies between the Γ and A k-points of the Brillouin zone. The calculated electronic structure around UVB can be attributed to the electronic states of AgS_4 tetrahedra and the region around the LCB can be attributed to the electronic states of BiS_6 octahedra. The S p-orbitals and Ag d-orbitals dominate the UVB and the Bi and S p-states dominates the LCB, respectively. As mentioned earlier, the forbidden transitions hints that the actual energy required for the electron to move from the VB to CB will be more than the computed bandgap value.

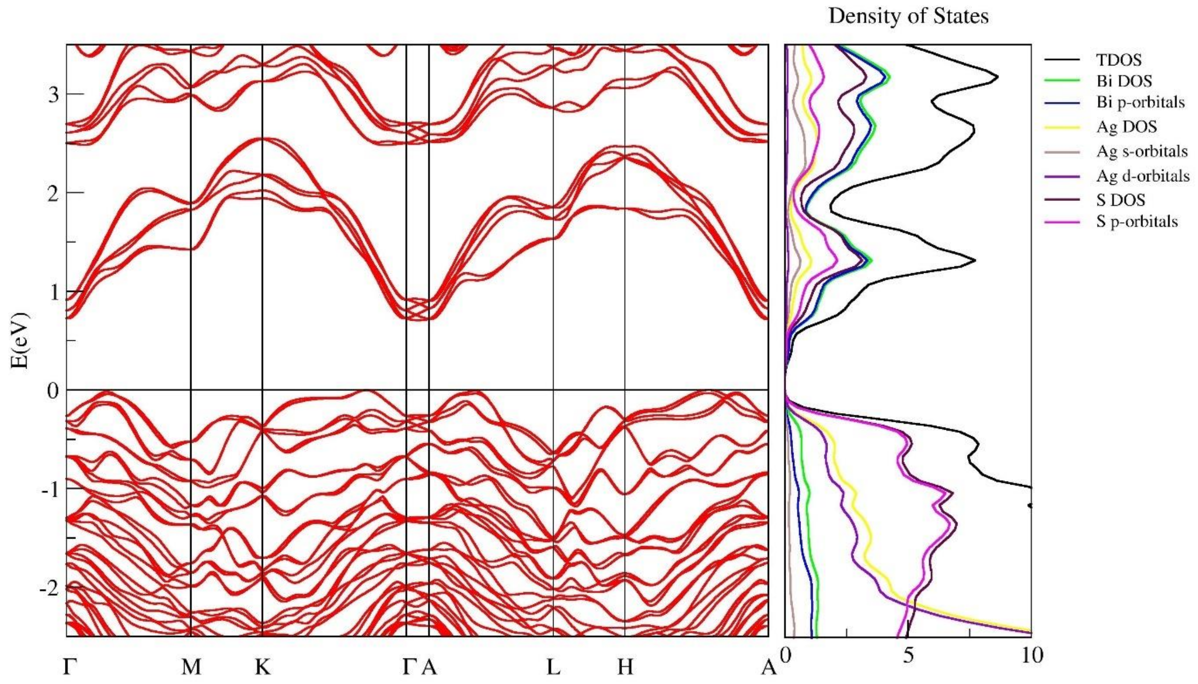

Figure 5. Optimised electronic structure of Silver bismuth sulphide. Calculated band structure for $AgBiS_2$. The valence band top is aligned at 0 eV (horizontal line) with the corresponding PDOS.

The imaginary part of the dielectric function was calculated using PBE-GGA to find out the energy value at which the actual electron transition starts. The calculations carried out using FHI-AIMS package were for an input light of energy range 0 to 7.5 eV that includes the infrared, visible and ultraviolet region of the electromagnetic spectrum. The first peak of the imaginary part of the dielectric spectra gives us the energy value at which the actual absorption takes place. The first peaks in the imaginary part of the dielectric function of TiO_2 and $AgBiS_2$ were found at 3.87 eV and 2.57 eV respectively and is shown in Figure 6. In the case of TiO_2 and $AgBiS_2$, the light absorption spectrum is isotropic along the x and y directions.

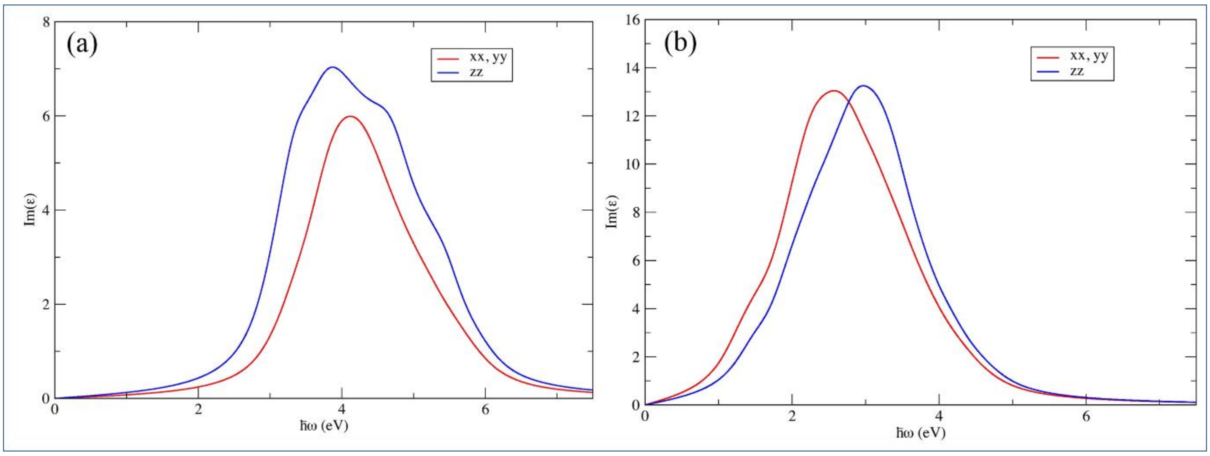

Figure 6. Imaginary part of the frequency-dependent dielectric function of (a) TiO_2, (b) $AgBiS_2$. Optical isotropy was found in the case of TiO_2 and $AgBiS_2$.

3.2. X-ray diffractogram (XRD)

The crystal structure of as synthesised $AgBiS_2$-TiO_2 composites was examined using XRD. Figure 7 shows the formation of the cubic phase of $AgBiS_2$ with a lattice constant of a= 5.64 Å is distinctly observed without formation of any impurity phase.[44] Well defined peaks at 27.5˚, 31.70˚, 45.79˚, 54.2˚, 56.4˚, 66.22˚ corresponding to (111), (200), (220), (311), (222) and (400) respectively is observed [JCPDS- 00-004-0699]. Figure S1 compares the as prepared $AgBiS_2$ with other standard peaks of Bi_2S_3 [JCPDS - 00- 017-0320] and Ag_2S [JCPDS- 00-033-0624]. This confirms the formation of a pure phase of silver bismuth sulphide without any impurities. In order to understand the optimum parameters for the solvothermal synthesis of $AgBiS_2$, different temperature and time studies were completed. Figure S2a and S2b illustrate the diffractograms obtained after synthesis at different temperatures and time respectively. As observed, in Figure S2a the crystallinity of the signature peak of $AgBiS_2$ at 31.7˚ increases with increase in temperature from 160 ˚C to 180 ˚C for a time of 24 h. The intensity of the same peak dampens on enhancing the temperature beyond 180 ˚C (at 200˚C). Similarly, in Figure S2b shows a similar pattern, on synthesising at 180 ˚C for different time periods, on increasing the time from 6 h to 24 h, the signature peak emerges gradually, while increasing it up to 48 h, decreases the crystallinity. The optimum solvothermal synthesis parameter for $AgBiS_2$ is 180 ˚C at 24 h.

Additionally, Figure 7 exhibits the formation of pristine anatase phase of TiO_2 [a=b= 3.7821 Å and c= 9.5 Å] with sharp peaks at 25.4˚, 38.5˚, 48.0˚, and 55.0˚ owing to (101), (112), (200) and (211) respectively.[45] The figure also illustrates the diffractograms of $AgBiS_2$-TiO_2 composites. As observed the peaks of $AgBiS_2$ is not evident at lower dopant percent (0.5 to 2 wt %). However, a small peak at 31.7° is observed in the case of 5 wt% $AgBiS_2$-TiO_2 composite.

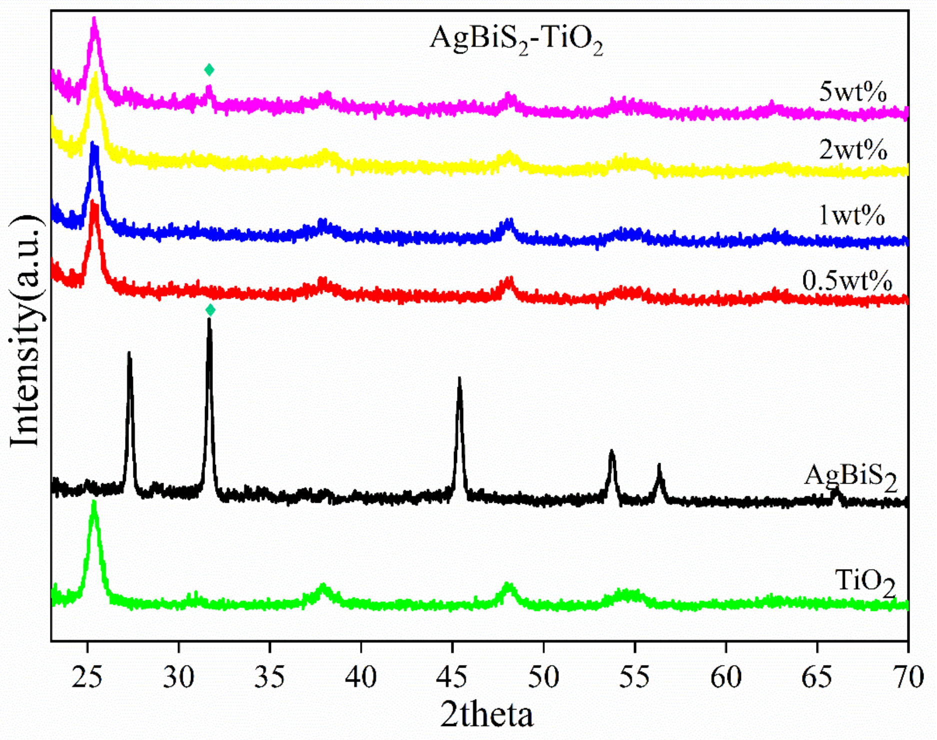

Figure 7. XRD patterns of as prepared TiO_2, $AgBiS_2$ and $AgBiS_2$-TiO_2 composites.

The most notable fact about the composites structures as observed in Figure 7 is that on the introduction of TiO_2 by solvothermal synthesis to form a possible heterojunction did not tamper the anatase phase of the sample and the crystallinity of the composite remained unaltered. The lattice constant obtained for pristine parent samples showed good agreement to the theoretically calculated values.

Similarly, as observed from the XRD diffractograms the formation of the metastable cubic phase of $AgBiS_2$ could be attributed to the choice of solvent used in the synthesis process. Ethanolamine (EA), with a single amine and N-chelating atom, has been used as a potential structure directing agent.[46] The inbuilt pressure and the appropriate temperature supports the formation of such unique phases. The growth mechanism of $AgBiS_2$ in a solvothermal technique could be explained as below;

$$AgNO_3 + EA \rightarrow Ag(EA)_x^+ + NO_3^- \text{ (Equation 6)}$$

$$Bi(NO_3)_3 + EA \rightarrow Bi(EA)_y^{3+} + 3NO_3^- \text{ (Equation 7)}$$

At the beginning of the reaction, the use of EA as solvent results in coordination with Ag^+, and Bi^{3+} ions to form a covalent complex as given above (where x and y are positive integers).[47, 48] Furthermore, these complexes react with thiourea (TH) to form complexes as;[49]

$$Ag(EA)_x^+ + xTH \rightarrow [Ag(TH)_x]^+ + EA \text{ (Equation 8)}$$

$$Bi(EA)_y^{3+} + yTH \rightarrow [Bi(TH)_y]^{3+} + EA \text{ (Equation 9)}$$

The solvent ethanolamine in the reaction aids in the formation of complexes in the first half of the reaction and also preserves thiourea from dissociation to form any free radicals of S^{2-}. This mechanism prevents the formation of any other impurity phases (binary compounds) such as Bi_2S_3 or Ag_2S. As the temperature enhances, the stability of the thiourea decreases to yield $AgBiS_2$, since the ternary chalcogenide is the more stable phase in that reaction atmosphere. In the meantime, thiourea in the reaction mixture plays a dual role in forming a complex and also being the source of sulphur.[50, 51]

$$[Ag(TH)_x]^+ + [Bi(TH)_y]^{3+} \rightarrow AgBiS_2 \text{(Equation 10)}$$

The 2 wt% $AgBiS_2$-TiO_2 composite illustrated the best photocatalytic results (discussed in the rest of the sections) among their parent and sister samples (of other dopant %) and hence hereafter are used for further characterisations unless otherwise stated.

3.3. Raman Spectroscopy

Figure 8 illustrates the Raman peaks of TiO_2, $AgBiS_2$ and $AgBiS_2$-TiO_2. In the case of $AgBiS_2$, a peak around 147 cm^{-1} is observed, which is assigned to the Ag lattice vibrations. A small peak at 238 cm^{-1} is attributed to the Ag-S lattice vibrations.[52, 53] Meanwhile, the typical active modes for anatase are observed at 147, 197, 396, 516 and 638 cm^{-1} for A1g, 2B1g and 3Eg respectively.[54, 55] On the other hand, for the composite samples, the peaks of anatase appears to be sharp and symmetric. A minor red shift is observed (as given in the inset of Figure 8a), as the peak maxima for the composite sample shift towards lower wavenumbers. This is considered to be the positive note of successful composite formation.[56, 57]

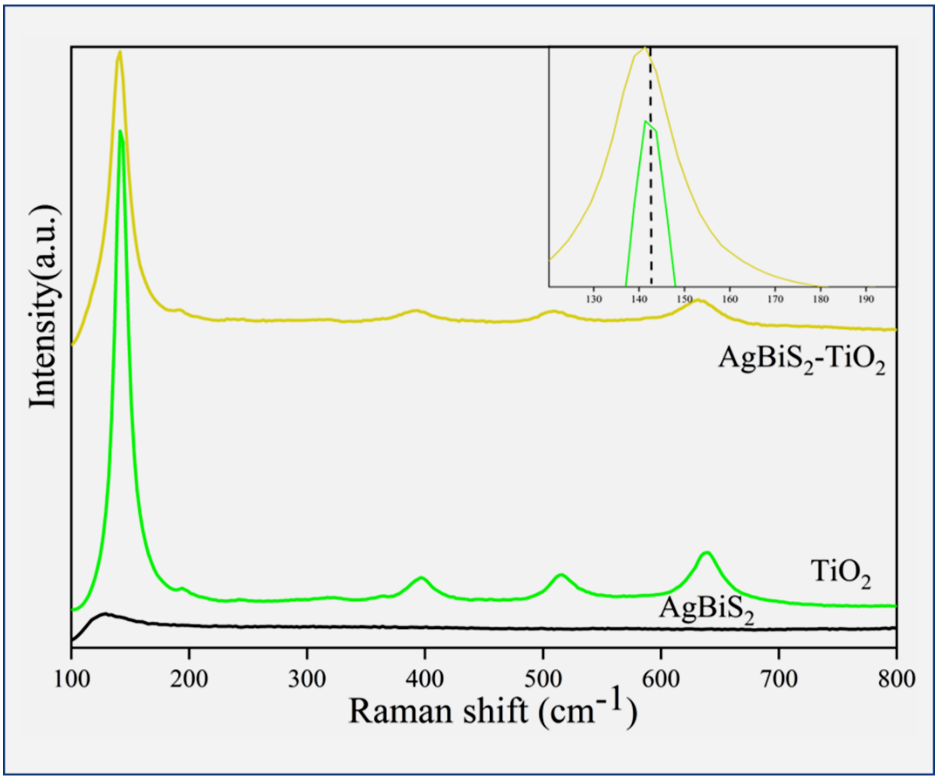

Figure 8. Raman spectra of TiO_2, $AgBiS_2$ and $AgBiS_2$ –TiO_2 composite.

3.4. X-ray Photoelectron Spectroscopy (XPS)

The chemical states and the nature of the bonds are detected by XPS. The survey spectra of TiO_2 and $AgBiS_2$-TiO_2 are given in Figure S3. Peaks of Ti 2p and O 1s are observed for TiO_2. Additional peaks of Ag 3d and Bi 4f are observed in $AgBiS_2$-TiO_2. Small peaks of C 1s and N 1s is also observed in all the samples which are presumably contaminants acquired during the synthesis or characterisation process.

Figure 9A shows the Ti 2p spectra of TiO_2 (a) and the composite sample (b). As observed, Ti 2p spectrum illustrates peaks of Ti $2p_{3/2}$ at 457.8 eV, which is consistent with Ti being in the +4 oxidation state. Similarly, Figure 9B illustrates the O 1s spectra of TiO_2 (a) and composite (b) sample. Peaks at 528.59 eV and 530.40 eV corresponding to the crystal lattice oxygen (O-Ti^{4+}) and for hydroxyl molecules respectively are observed. There is no evident shift in peaks of Ti 2p and O 1s of the composite sample.[45, 58, 59] Figure 9C exhibits the high-resolution spectra of Ag 3d spectra of $AgBiS_2$ (a) and composite (b) sample. Characteristic peaks of Ag $3d_{3/2}$ and Ag $3d_{5/2}$ are observed at 373.9 eV and 367.9 eV respectively for $AgBiS_2$.[60, 61] A shift of approximately -1.8 eV is observed in the peaks of Ag $3d_{3/2}$ and Ag $3d_{5/2}$ [372.03 eV and 366.04 eV respectively] of $AgBiS_2$–TiO_2 composite sample. Similarly, Figure 9D illustrates the high-resolution spectra of Bi 4f and S 2p spectra for $AgBiS_2$ (a) and composite (b) sample. The characteristic peaks at 163.66 eV and 158.28 eV corresponding to the Bi $4f_{5/2}$ and Bi $4f_{7/2}$ respectively is observed for $AgBiS_2$ with a doublet separation of 5.38 eV.[60-62] The S 2p peaks of the pristine $AgBiS_2$ sample is assigned at 161.12 eV.[19, 60] The composite sample illustrates the presence of Bi in +3 and elemental oxidation states. The peaks at 155.24 eV and 160.60 eV corresponds to the Bi in elemental state, while the peaks at 157.13 eV and 162.57 eV corresponds to the Bi in +3 oxidation states of $AgBiS_2$.[62, 63] The doublet splitting remained consistent (~5.4 eV) for both the oxidation states. Moreover, as in the case of Ag 3d, the peaks of Bi 4f of the composite also exhibited a considerable shift of -1.1 eV. The summarised glance of the position of all the elements is tabulated in Table S1. As observed in the case of the composite structure, the shift in the peaks of Ag and Bi compared to their pristine samples is evident. The binding energy shifts of the heterostructure components is explained by the strong interaction between $AgBiS_2$ and TiO_2. The increase in electron concentration due to strong electron screening effect results to the decrease in binding energy. Whereas the decreased electron concentration by the weakened electron screening effect leads to increase in binding energy. Therefore, in the current aspect the increase in electron concentration due to the interfacial charge transfer between heterostructure components result in the shift of the peak observed.[64-67]

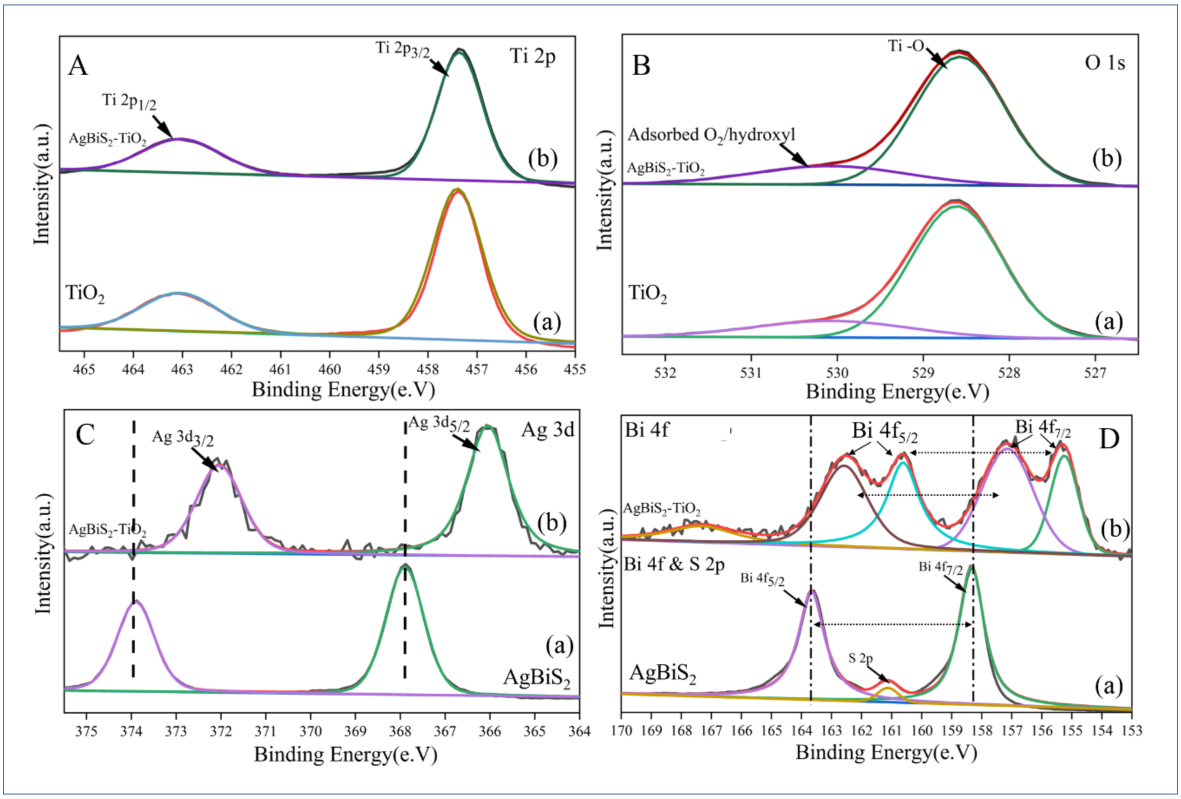

Figure 9. Deconvoluted spectra (A) high resolution spectra of Ti 2p (a) TiO_2 and (b) $AgBiS_2$-TiO_2; (B) high resolution spectra of O 1s (a) TiO_2 and (b) $AgBiS_2$-TiO_2; (C) high resolution spectra of Ag 3d (a) $AgBiS_2$ and (b) $AgBiS_2$-TiO_2 and (D) high resolution spectra of Bi 4f and S 2p (a) $AgBiS_2$ and (b) $AgBiS_2$-TiO_2.

3.5. UV-Vis absorption and bandgap estimation

The optical absorption, corresponding electron transition and the band gap of the as prepared samples were studied using UV-Vis spectra. On exposing semiconductor material with photons having energy greater than its band gap, an electron from the valence band (VB) transfers to the conduction band (CB). Hence, we observe an increase in absorbance at a corresponding wavelength (λ). The nature of the absorption coefficient (α), with the incident light, depends on the electronic transitions. During the electron transfer, if the momentum of the electron is conserved, then it is defined as a direct band semiconductor. While, if the momentum of the electron is not conserved, then there involves phonon in the process and defined as indirect band semiconductor.[68, 69]

On plotting $[h\nu F(R)]^{1/n}$ against hν, the tangent line is drawn along the slope of the spectra which intersects the horizontal axis provides the band gap value Eg. However, it should be noted that absorption is determined by low and high energies, when the photon energy is greater to the band gap (Eg) of the semiconductor, the absorption increases linearly with increase in photon energy.[70] While, the photon energy is lower than Eg, then the absorption observed deviates from linearity and exhibits photonic absorption corresponding to the defect levels present in between the VB and CB of the sample.[71]

Figure 10 shows the diffuse reflectance spectra and band gap estimation of TiO_2 and $AgBiS_2$-TiO_2 composites. A sharp absorption at UV region (350 nm) is observed by TiO_2 while a significant enhancement in the visible light absorption is observed for the composite samples (Figure 10a). As observed, all the composite samples exhibit the absorption shoulder at 380 nm, the signature peak of TiO_2 but the absorption edge of all the spectra are enhanced up to 800 nm. This shows the improved visible light absorption observed in composites samples at a very small addant levels. Meanwhile, Figure 10b illustrates the corresponding indirect band gap energies of the samples. As perceived, the band gap values of TiO_2, and $AgBiS_2$- TiO_2 is estimated as 3.18 eV and further decreases with increase in $AgBiS_2$ content (as given in the inset of Figure 10b).

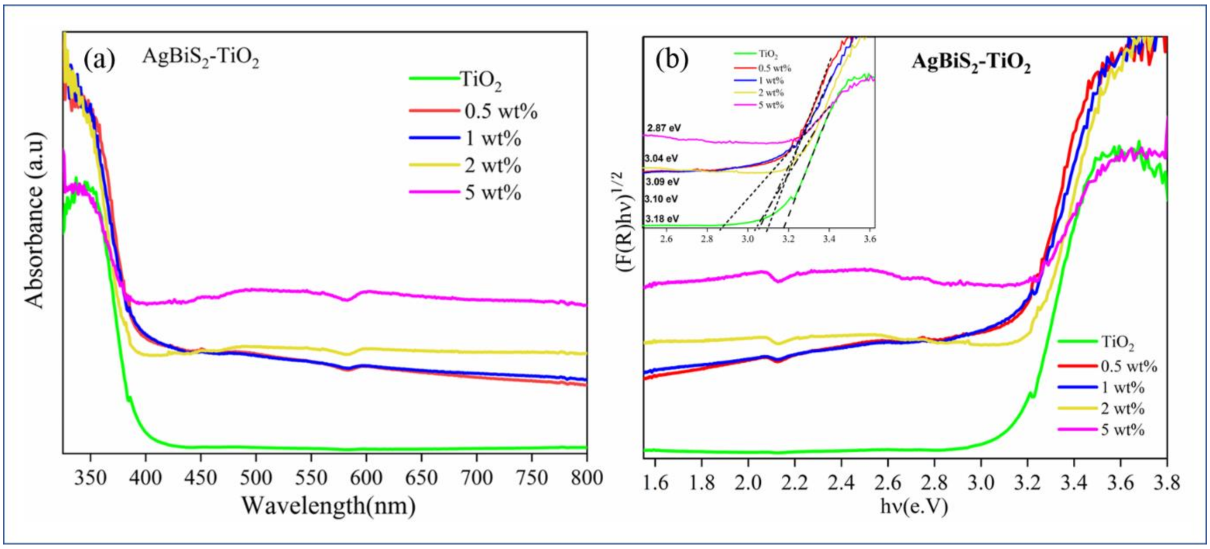

Figure 10. (a) DRS spectra and (b) band gap estimation of TiO_2 and AgBiS2-TiO_2 composites.

In the case of pristine $AgBiS_2$, a defined absorption peak is observed around 380 nm (Figure 11a). Apart from that, Figure 11b illustrates the direct band gap calculated from the Kubelka-Munk plot.[72] The Table S3 tabulates the obtained band gap values of TiO_2 and $AgBiS_2$-TiO_2 composites.

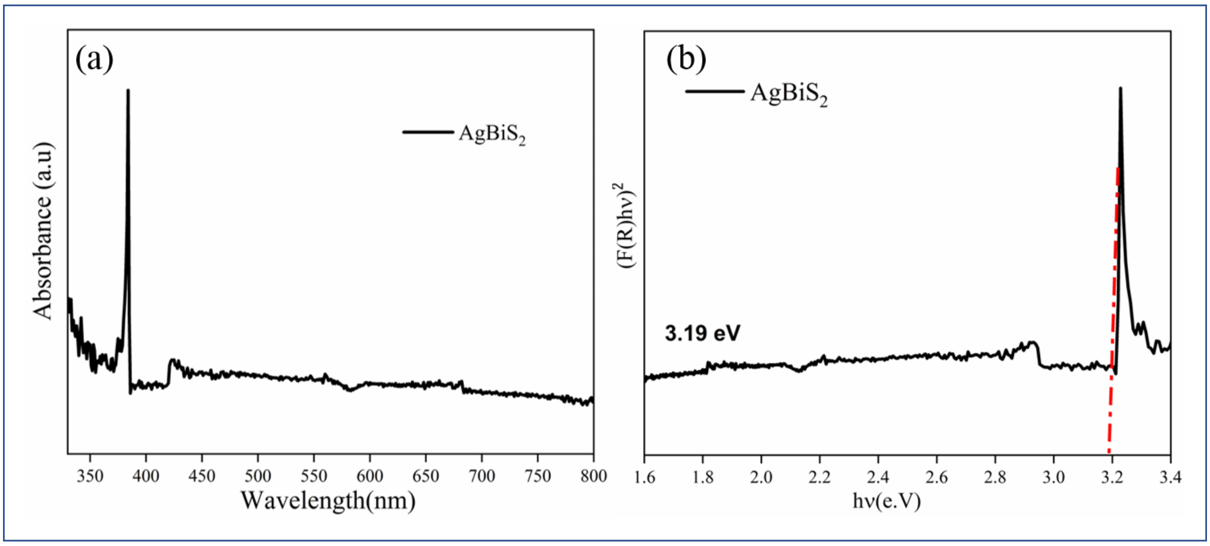

Figure 11. (a) DRS spectra and (b) band gap estimation of $AgBiS_2$.

The absorption edge of the pristine TiO_2 nanoparticles in the DRS spectra is observed around 415 nm while the $AgBiS_2$ shows an absorption edge around 400 nm. However, a strong visible light absorption extending up to 800 nm is observed in case of $AgBiS_2$. The composite samples, exhibits strong absorption of TiO_2 and illustrates an enhanced absorption edge garnered by the increased visible light absorption due to the coupling with $AgBiS_2$. It is in good agreement with the change in colour of the composite sample from white (TiO_2) to dark grey (2 wt% $AgBiS_2$-TiO_2). As observed in XPS results, the strong interaction between the heterostructure components leads to interfacial electron transfer which results to the enhanced absorption edge and decrease in the overall band gap.[64, 66, 67]

3.6. Transmission Electron Microscopy (TEM)

The morphology and the details of the microstructure formed are evaluated using transmission electron microscopy (TEM). Figure 12a illustrates the TEM image of TiO_2 and its SAED pattern. The nanoparticles where spheroidal in nature and were of the average size of 25 to 40 nm. The anatase phase of the nanoparticles formed is evident from the *d* spacing values calculated for different zones.[73] The TEM image of $AgBiS_2$ is observed in Figure 12b, these nanoparticles also appeared to be spheroidal in nature. The lattice fringes of planes (111), (200) and (220) with corresponding *d*- values of 0.324 nm, 0.282nm and 0.198 nm is observed.[74] Meanwhile, Figure 12c and 12d show the TEM images of the $AgBiS_2$-TiO_2 composite. The image shows the presence of irregular particles identified as $AgBiS_2$ (through lattice fringe identification).[44] The low dopant ratio of the ternary chalcogenides makes them difficult to be observed. However, the presence of the $AgBiS_2$ nanoparticles demonstrates the successful integration with the TiO_2 nanoparticles firmly and hence forming heterojunction structures. Figure S4 in supporting information displays some additional TEM images of $AgBiS_2$-TiO_2 composite structure.

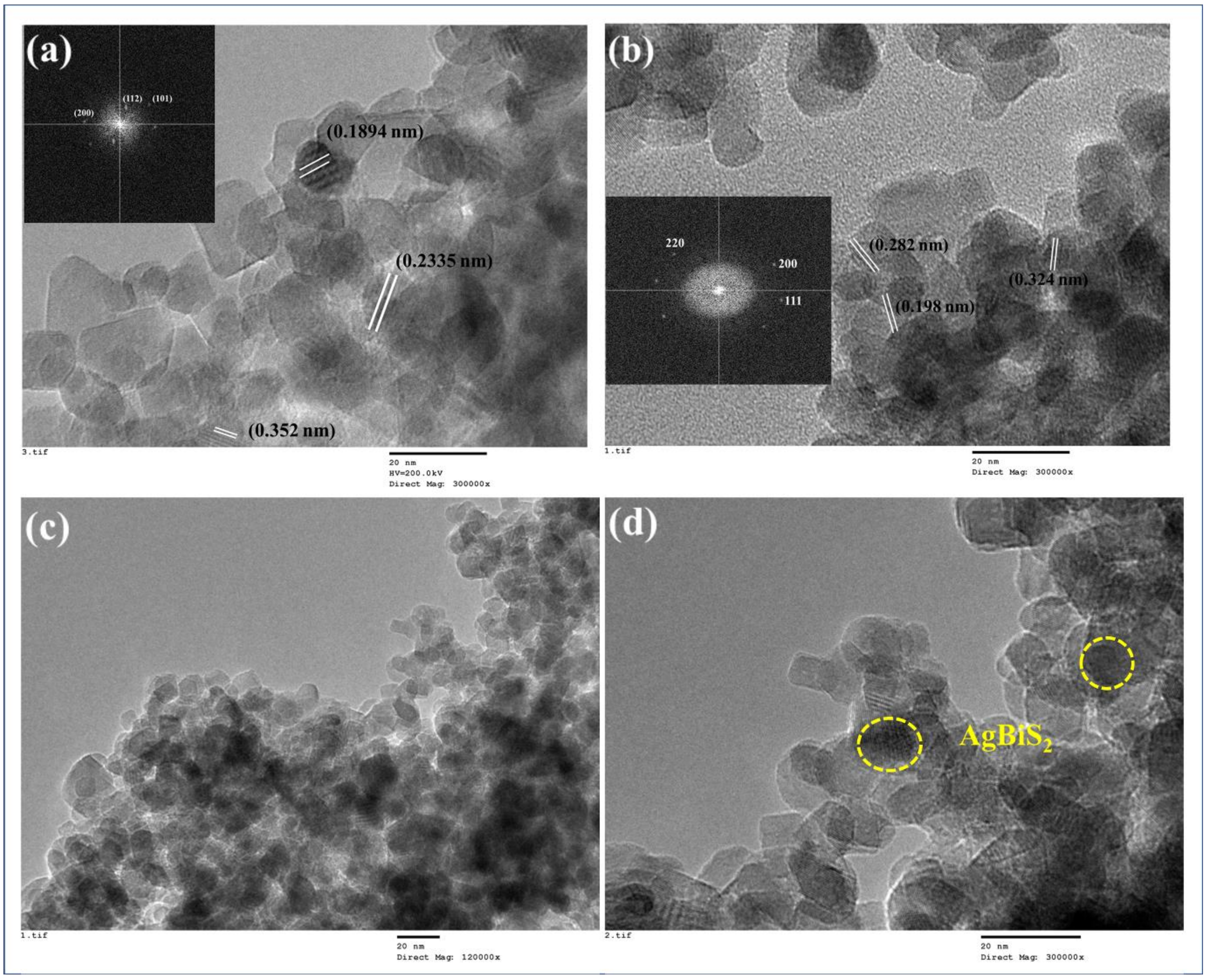

Figure 12. TEM images of (a)TiO_2; (b)$AgBiS_2$; (c) and (d) $AgBiS_2$-TiO_2 composite.

3.7. Photodegradation

The discharge of pharmaceutical effluents and hospital residues into the aquatic streams is considered as one of the major routes for the growth of drug-resistant bacteria and other organism.[75] The photocatalytic efficiency of the as synthesised TC composites with TiO_2 was evaluated by degradation of Doxycycline (DC) as a modal pollutant and compared with their pristine parent samples. The photocatalytic experiments were conducted under dark and light illumination respectively. The composites and their parent samples did not show any adsorption activity in all the cases. Figure 13 illustrates the degradation profile of $AgBiS_2$-TiO_2 composites by showing the change in concentration of DC with time [C/C_0 % vs time]. As observed, the parent samples $AgBiS_2$ and TiO_2 with higher band gap values show the least activity. On the other hand, the composites samples show more than 94% degradation within

180 min of irradiation. The 5 wt% composite exhibited the least and the 2 wt% composite showed the best degradation activity among the entire composite sample. This proves that the composites show better results only at lower dopant levels, and the activity decreases as the loading levels go higher than 2 wt%. a bandgap value of 1.95 eV was not efficient to show improved activity. This could be attributed to the high recombination of the photogenerated electron-hole pairs. These results could be further validated by the H_2 production results as discussed in section 3.8.

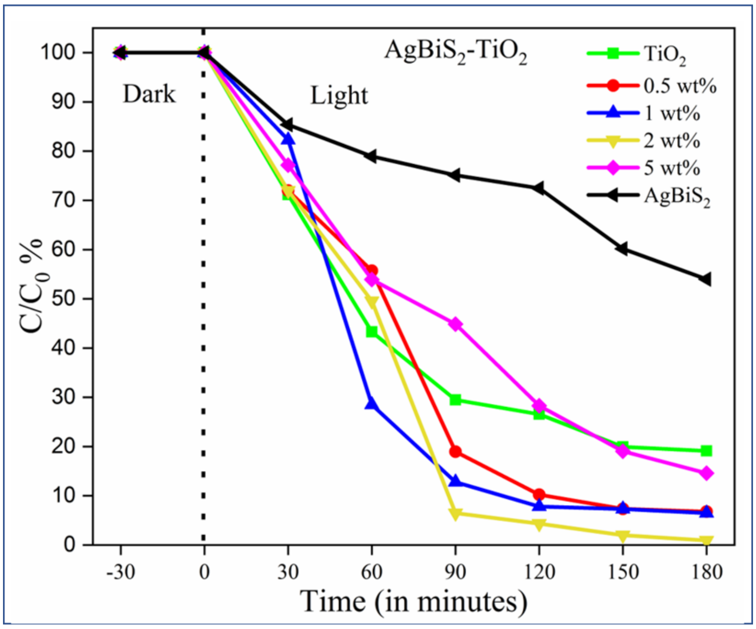

Figure 13. Change in concentration of DC with time TiO_2, $AgBiS_2$ and $AgBiS_2$-TiO_2 composites.

The photocatalysts after every single photocatalytic study were washed, dried and reused to evaluate the recyclability of the efficiency of the samples. Figure 14 illustrates the recyclability profiles of 2 wt% $AgBiS_2$-TiO_2. As observed, the efficiency of the samples remains consistent even after 4 cyclic runs.

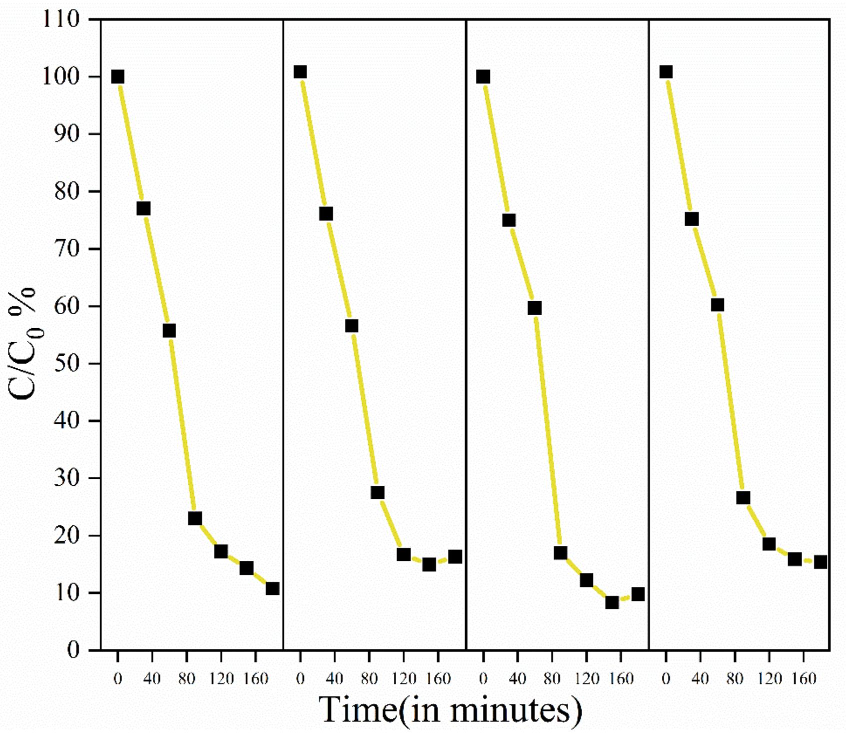

Figure 14. Recyclability profiles of 2 wt% $AgBiS_2$-TiO_2.

The scavenging experiment was also performed to evaluate the potential reactive oxygen species involved in the degradation process by adding $AgNO_3$, triethanolamine, benzoquinone and IPA in the reaction mixture.[76] Figure S5 compares the degradation percent of all the 4 set of systems with 2 wt% $AgBiS_2$-TiO_2 in the reaction mixture on exposed for 180 min of light irradiation. Electrons and holes are found to be the major reactive species in this case, as the reduction activity was affected significantly on the addition of $AgNO_3$ and benzoquinone (BQ). However, the system with IPA showed a slight reduction, which apparently proves that hydroxyl radicals did not have a much significant role in the degradation reaction. Hence, electron and holes could be found as the major species for $AgBiS_2$-TiO_2. The photocatalytic degradation and the possible intermediates (polar and non-polar) formed has been identified using GC-MS and HPLC-MS [77]. Based on the chromatograms obtained Zhu *et al*. proposes a degradation pathway (Figure 15).[77] The holes generated in the process accepts electrons from the pollutant molecules and results in formation intermediate products. The loss of N-methyl group was observed at the very beginning, which resulted in an anion species of m/z 431. Further degradation results in formation of intermediates at m/z 400. Additional mineralisation after a prolong irradiation results in the breakdown of the DC structure and results in generation of smaller fragments of complex structures. Further oxidation of these complex structures leads to generation of shorter organic compounds such as acids and alcohols.[77-79]

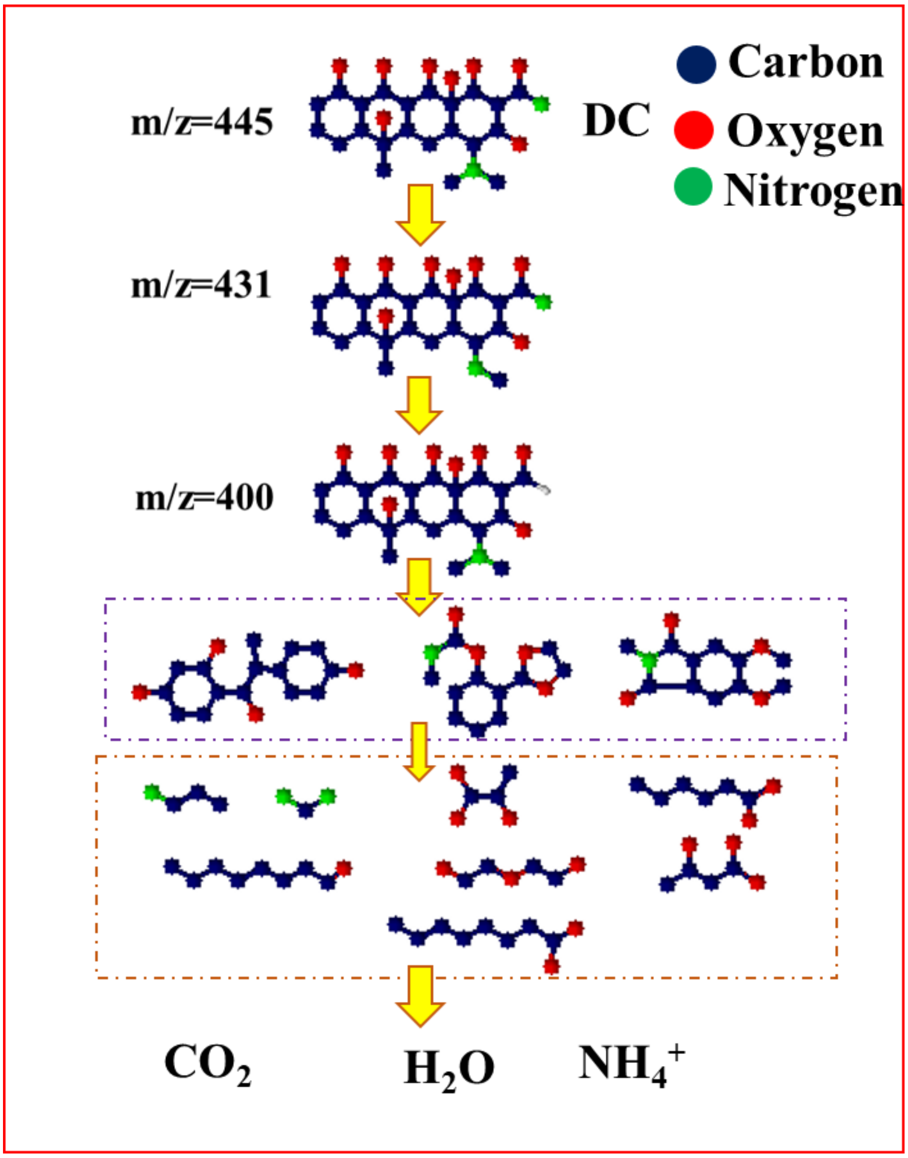

Figure 15. Schematic illustration of a plausible photocatalytic degradation pathway of Doxycycline.[77, 78]

3.8. Photocatalytic H_2 production

In order to evaluate the photocatalytic efficiency, the as prepared composites of TC with TiO_2 was studied for hydrogen production. The use of photocatalytic water splitting and photoreforming has been considered as a vital process to convert solar energy into the chemical. The use of sacrificial organic agents in water splitting process can aid in photoreforming by simultaneously reacting with the photogenerated positive holes to oxidize organic species and produce hydrogen ions. The electrons photogenerated on the catalyst surface react with the H^+

ions to yield hydrogen gas. Thus, combining organic wastewater management and hydrogen production using solar energy could be a promising alternative strategy.

The hydrogen production rate of $AgBiS_2$-TiO_2 composite samples along with their pristine parent materials was evaluated in the presence of methanol ($[CH_3OH]$ =10 vol.%) as sacrificial species. As it is clear from the figure illustrated (Figure 16a), all the catalyst tested showed an almost negligible hydrogen production in the first 60 minutes of reaction, during which the UVA-component of the light source was cut off by means of a proper sodium nitrite filter, as reported in Section 2.6. After removing the UVA-cut off filter, the highest values of hydrogen production rate for the $AgBiS_2$-TiO_2 materials were recorded over weight percentages of 0.5, 1 and 2 wt%. Lower values of hydrogen production rate were recorded for the 5 wt% $AgBiS_2$-TiO_2 sample, thus showing that on increasing the doping levels beyond 2%~~,~~ the efficiency of the process decreases. The composite structures at lower weight percent exhibited H_2 production as high as 1310 μmole/min, compared to almost 0 μmole/min observed in case of the parent pristine samples ($AgBiS_2$ and TiO_2). With regard to the solution pH, no significant changes were recorded for the $AgBiS_2$-TiO_2 samples throughout the reaction time, with the exception of the 2 wt% $AgBiS_2$-TiO_2 sample, for which a moderate pH decrease was observed after removing the UVA-cut off filter (Figure 16b).

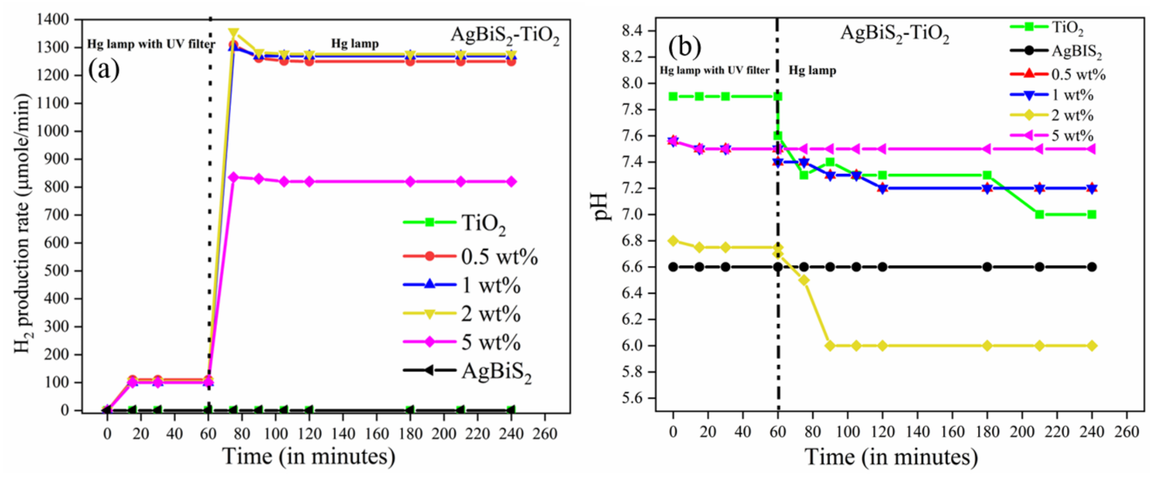

Figure 16. (a) The H_2 production rate and (b) pH of the solution at varying weight percentage of $AgBiS_2$-TiO_2 catalysts. $[CH_3OH]$ =10 vol.%; Catalyst load=500 ppm; T=25°C; P=1 atm.

While Figure 17a shows the irradiance, values recorded in the UV range (λ=315÷400 nm) on the external wall of the reactor in the first 60 minutes of reaction are almost negligible due to the presence of the UVA-cut off filter. After removing the UVA-cut off filter, an instant increase in the irradiance values was recorded, which was followed by a moderate lowering at t=90 min probably due to the photocatalysts activation resulting into a higher suspension absorption. No significant changes before and after removing the UVA-cut off filter were observed for the irradiance values collected on the external walls of the reactor in the visible range (λ=400÷1100 nm) as shown in Figure 17b. The higher values recorded for the 5 wt % $AgBiS_2$-TiO_2 sample indicate its lower capability to absorb the light irradiation in the visible range.

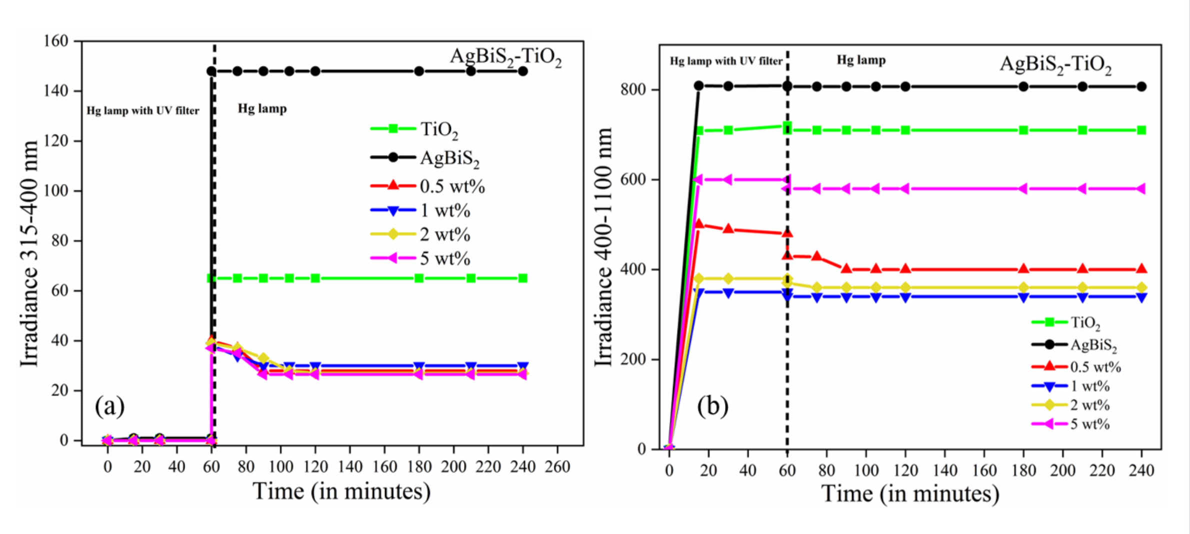

Figure 17. Irradiance measured on the external walls of the reactor between (a) 315-400 nm and (b) 400-1100 nm at varying weight percentage of $AgBiS_2$-TiO_2 catalysts. [CH_3OH]=10 vol.%; Catalyst load=500 ppm; T=25°C; P=1 atm.

3.9. Photocatalytic antimicrobial studies

The evaluation of photocatalytic bacterial inactivation of *E. coli* and *S. aureus* to $AgBiS_2$-TiO_2 samples was carried out by suspension test. The solutions of catalyst were prepared in distilled water, inoculated with bacterial strains and further subjected to dark and light conditions respectively. Control samples were prepared without the addition of catalysts. The obtained data were also compared with their parent samples. Exposing the bacterial cells with catalysts (1 g/L) under visible light, showed different results. The composite structure displayed a superior photocatalytic efficiency than that of pristine samples [$AgBiS_2$ & TiO_2], under light irradiation. In the absence of photocatalysts, the growth of both strains was the same under light and dark conditions. Graphical representation of the test results of $AgBiS_2$-TiO_2, $AgBiS_2$ & TiO_2 against *E. coli* and *S. aureus* is given in the above Figure 18.

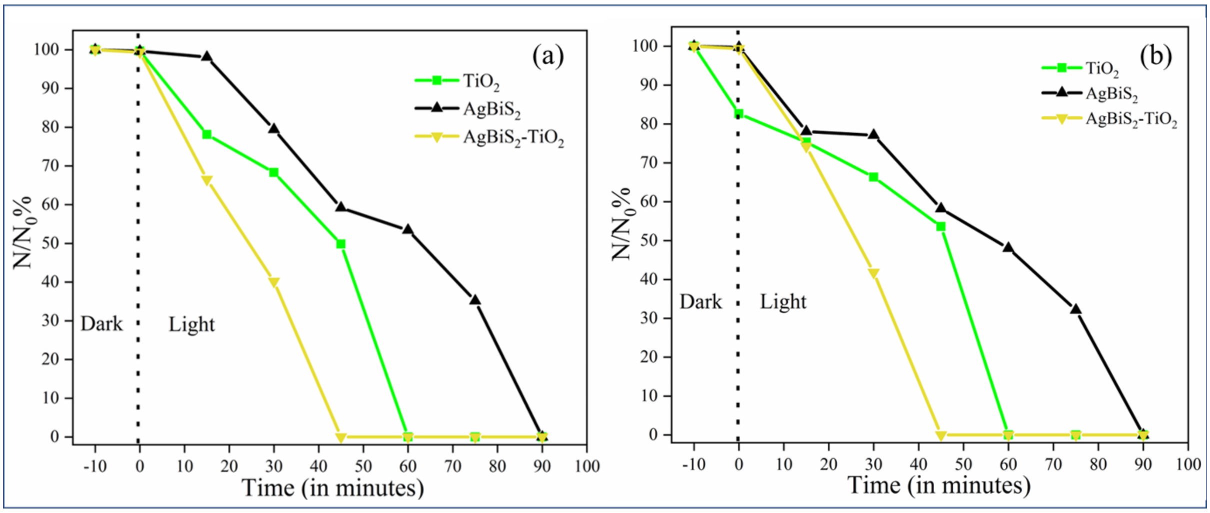

Figure 18. Photocatalytic inactivation of (a) E. coli and (b) S. aureus with TiO_2, $AgBiS_2$ and $AgBiS_2$-TiO_2.

For both the strains, all the catalysts exhibited a similar pattern of photocatalytic activity. In the case of $AgBiS_2$-TiO_2, a visible decrease was observed in the bacterial growth for both the strains. Log 3 reduction was attained within 45 min of irradiation (Figure S6). While, for pristine $AgBiS_2$, it required 90 mins of exposure to achieve the same result. Figure 19 illustrates the images of bacterial colonies grown on agar plates on various time intervals for $AgBiS_2$-TiO_2.

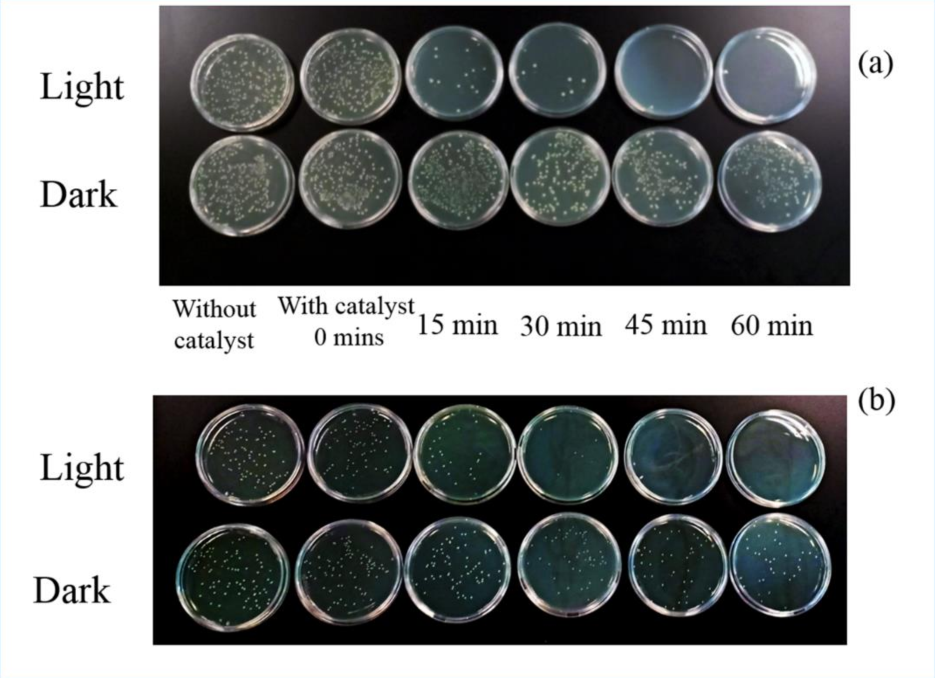

Figure 19. Images of (a) *E. coli* colonies and (b) *S. aureus* colonies on agar plates after various time intervals of $AgBiS_2$-TiO_2.

The close interface developed in the composite structure aided to the delayed charge recombination. Thus promoting the inactivation efficiency amongst the composite sample when compared to their parent samples. The charge carriers results in formation of potential reactive oxygen species which tampers the bacterial cell wall integrity. This results in outflow of intracellular materials and cell lysis. Moreover, the reactive species created in the photocatalytic process has the ability to cause gene alteration by oxidation of the DNA. Alteration in the genetic expression would affect the cellular functioning and could lead to cell lysis. [30, 80]

3.10. Photoluminescence analysis

The mass normalised photoluminescence spectrum of TiO_2 and composites of $AgBiS_2$-TiO_2 is presented in Figure 20. It is used to demonstrate the effect of heterojunction formation on the exciton recombination rates. The emission peak of $AgBiS_2$-TiO_2 shows dampened intensity compared to TiO_2. The lower PL intensity indicates the lower recombination of electron-hole pairs. The recombination of the excitons was inhibited by the heterostructure formation, resulting in high photocatalytic efficiency. On the other hand, the strong fluorescence signals observed in the case of TiO_2 is due to the higher rate of recombination, which further explains the lower photocatalytic activity observed.

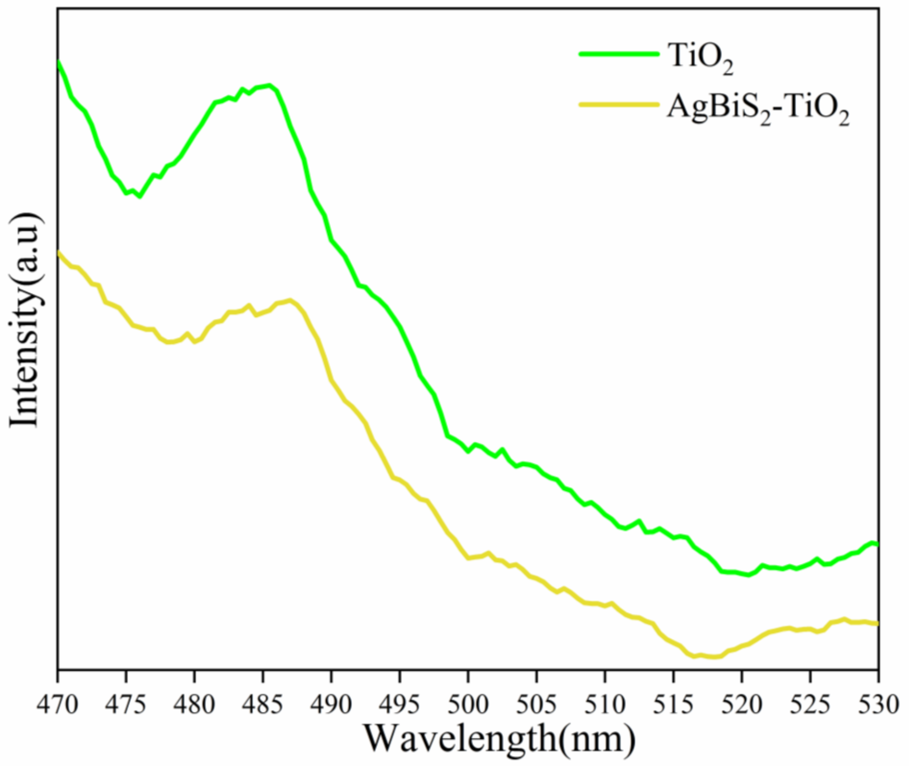

Figure 20. The photoluminescence spectra of TiO_2 and composites of $AgBiS_2$-TiO_2.

4. Photocatalytic Mechanism

All the above applications demonstrated that the composite architecture of ternary chalcogenide with TiO_2 showed impressive results compared to their pristine parent samples. The theoretical study was important to understand the electronic and optical properties of this ternary chalcogenide along with TiO_2. The TC exists in polymorphic states as discussed in the introduction and also found in theoretical studies. The computational analysis reveals the stability of trigonal crystal structure of $AgBiS_2$, while positive formation energy is observed in the case of the cubic phase of the sample. The use of solvent like ethanolamine, as explained in section 3.2, plays crucial role in stability as well as the formation of such metastable phases. Moreover, the band structure and PDOS analysis reveal that the valence band of TiO_2 is dominated by Ti 3d orbital and the CB is governed by the 2p orbital of oxygen. On visible light irradiation on $AgBiS_2$-TiO_2 composites, the electrons travel from the Ag 4d and S 3p orbitals to the Bi 3p orbital of $AgBiS_2$ respectively, and further to the O 2p orbital of TiO_2.

The XPS results highlight the shift of the TC peaks in composite structure to lower binding energies. The strong interaction between the heterostructure components, resulted in the shift. However, the peaks of TiO_2 remained unaltered, when compared with the parent and the composite sample. In the composite sample, the presence of peak at 457.8 eV is the direct measure of the Ti in +4 state. It also indicates the absence of any increase in anionic oxygen vacancies in the heterostructure formed. The strong Ti^{+4} state reiterates the anatase phase of the sample in the composite architecture, which effectively contributes to the photocatalytic process.[32, 58] Apart from that, it is further observed in all the application results that the TC at lower dopant ratio effectually contributes to the degradation/disinfection and the H_2 production output. However, on enhancing the dopant concentration beyond an optimised limit, results in suppression of the effective interfacial charge transfer, as these dopant sites start to behave as potential recombination centres.[81-83]

On the basis of the theoretical study, scavenger experiments, band gap values from UV-DRS and the PL results, a likely photocatalytic mechanism is illustrated for $AgBiS_2$-TiO_2. In order to understand the separation of photogenerated e-hole pairs over the two different nanocomposites, it is vital to calculate the CB and VB potentials of the components. The energy levels are calculated using the following empirical equations;[41]

$$E_{VB} = \chi - E^e + 0.5\, E_g \text{ (Equation 11)}$$

$$E_{CB} = E_{VB} - E_g \text{ (Equation 12)}$$

Where, χ= Mulliken's electronegativity

E^e= Energy of a free electron on hydrogen scale (ca. 4.5 eV)

E_g= Band gap of the semiconductor

E_{VB}= Valence band potential of the semiconductor

E_{CB}= Conduction band potential of the semiconductor

Now, according to Mulliken's electronegativity theory, electronegativity (χ) of any element is the arithmetic mean of the first ionisation energy (I.E) and the electron affinity (E.A) of an element:[84, 85]

$$\text{so, } \chi = \frac{1}{2}[I.E + E.A] \text{ (Equation 13)}$$

and χ of any polyvalent molecule say $A_aB_aC_c$ is given as;

$$\chi_{AaBbCc} = [(\chi_A)^a \times (\chi_B)^b \times (\chi_C)^c]^{\frac{1}{a+b+c}} \text{ (Equation 14)}$$

where a, b and c are the number of atoms of A, B and C respectively.

Thus, to estimate the E_{CB} and E_{VB} values of TiO_2 and $AgBiS_2$, it is important to estimate the χ_{TiO2} and χ_{AgBiS2}. In order to do so, the E.A and the I.E values of constituent elements are provided in Table 1

Table 1. I.E and E.A values of elements

Elements	I.E (eV)	E.A (eV)
Ti	6.82	0.079
O	13.618	1.46
Ag	7.576	1.301
Bi	7.289	0.945
S	10.36	2.07

Hence, using equation 14, the χ values of TiO_2 and $AgBiS_2$ are calculated. Table 2 summarises the χ values calculated and the Eg values obtained from the UV-DRS plot in section 3.5.

Table 2. χ values and E_g values.

Semiconductor	χ (eV)	Eg (eV)
TiO_2	5.805	3.18
$AgBiS_2$	5.1533	3.19

Hence using equation 11 and 12, the E_{CB} and E_{VB} of the bare samples are estimated. Table 3 summarises the values as obtained after calculation

Table 3. E_{VB} and E_{CB} values.

Semiconductor	E_{CB} (eV)	E_{VB} (eV)
TiO_2	-0.285	2.895
$AgBiS_2$	-0.9417	2.248

Thus, using the above calculated values, a possible photocatalytic mechanism is proposed below. In Figure 21, illustrates the band edge position of the CB and VB potentials of $AgBiS_2$ and TiO_2, before and after the formation of a possible $AgBiS_2$-TiO_2 nanocomposite heterojunction. The Fermi levels of $AgBiS_2$ and TiO_2 is located at 0.65 eV and -0.1 eV respectively (Figure 21a). As the heterojunction is created, the Fermi levels of both the semiconductors reach a uniform level.[86, 87] In this case, the band positions of $AgBiS_2$ is altered as it is in low dopant levels, so the Fermi level of $AgBiS_2$ reaches -0.1 eV, which is identical to that of TiO_2. Figure 21b shows the new band edge positions for $AgBiS_2$ as the VB and CB moves to +1.49 and -1.6917 eV. In this type-II heterostructure, on visible light illumination, electron hole pairs are generated on the surface of TiO_2 and $AgBiS_2$. The holes from the valence band of TiO_2 migrate to the VB of $AgBiS_2$ and the electrons migrate to the CB of titania. As explained in the XPS, the electronegativity difference between titania and $AgBiS_2$ nanoparticles and the band alignment in the heterojunction, promotes the transfer of the flow of electrons to the CB of TiO_2. These electrons react with the oxygen adsorbed in the catalyst surface to form superoxide radical and the holes participate in the reaction process directly. This explains the role of different ROS species, as suggested in the results observed in scavenger experiments. The scavenging results illustrated the superior role of superoxide radicals, electrons and holes in the enhanced photocatalytic applications. The ROS generated further undergoes the photocatalytic process.

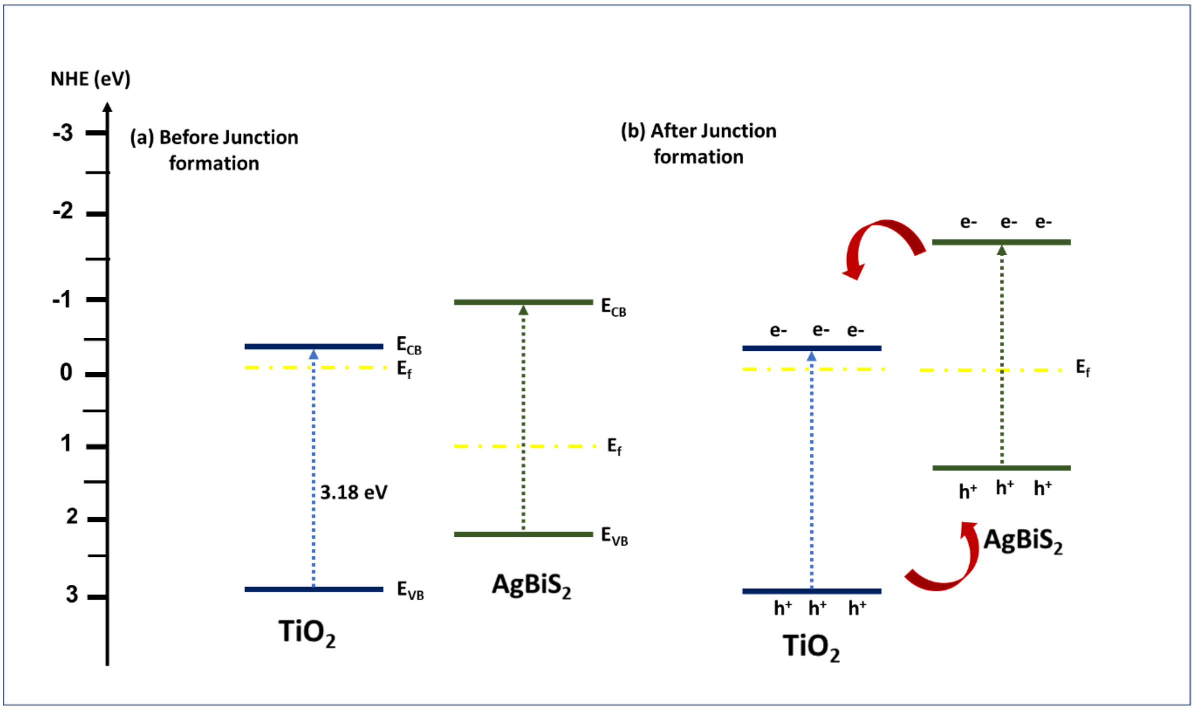

Figure 21. The photocatalytic mechanism for $AgBiS_2$-TiO_2.

5. Conclusions

In this study, we successfully synthesised $AgBiS_2$-TiO_2 using a one-pot solvothermal technique. The as a prepared composite structure with a small dopant level was efficient in improved visible light absorption. The band gap of the composites decreased with the increase in the dopant levels. Moreover, the XPS analysis demonstrated the shift in the peaks corresponding to the change in the local environment of the composite structure. The degradation results of the composites showed improved efficacy. Similarly, a significant improvement for the light induced hydrogen generation is also observed. A log 3 bacterial reduction was attained within 30 minutes of visible light illumination. A plausible mechanistic understanding is proposed based on computational analysis, scavenger experiments and the band gap values derived from the DRS plot. Thus, the present study demonstrates the successful formation of photocatalytic heterostructure for environmental remediation.

Supporting Information

XRD of temperature and time study of $AgBiS_2$. XRD of purity determination of TC by comparative assessment. Survey spectra of TiO_2, $AgBiS_2$-TiO_2. Tables summarising the peak positions of $AgBiS_2$ and $AgBiS_2$-TiO_2. Tables summarising the band gap values of TiO_2, $AgBiS_2$, and $AgBiS_2$-TiO_2 composites. Scavenger result of $AgBiS_2$-TiO_2 and the Log reduction of all the samples against *E. coli* and *S. aureus*.

Acknowledgement

PG and SK would like to acknowledge the Institute of Technology Sligo President's Bursary for providing financial support (grant no: PPRES052 and PPRES050 respectively). P.G., S.M., and S.P. would like to acknowledge access to Raman Spectroscopy and PL spectroscopy at Centre for Research in Engineering Surface Technology (CREST), FOCAS Institute, Dublin Institute of Technology, Kevin Street. The TEM imaging was carried out at the Advanced Microscopy Laboratory (AML) at the AMBER centre, CRANN Institute (www.crann.tcd.ie/Facilities/Advanced-Microscopy-Laboratory.aspx), Trinity College Dublin, Ireland. AML is an SFI supported imaging and analysis centre. S. K and A. A are grateful to Prof. Stefano Sanvito, Trinity College Dublin, for FHIAIMS package. Computational resources have been provided by the supercomputer facilities at the Trinity Centre for High Performance Computing (TCHPC) under the project code: HPC_16_00953 and Irish Centre for High-End Computing (ICHEC) under the project code: is-phy001c. PG would like to acknowledge Dr. Manu Jose for the JCPDS files. The authors would also like to extend sincere gratitude towards the referees for their valuable comments in improving the standard of the manuscript.

References

[1] M. Grätzel, Recent advances in sensitized mesoscopic solar cells, Accounts of chemical research, 42 (2009) 1788-1798.

[2] W.-J. Ong, 2D/2D graphitic carbon nitride (g-C3N4) heterojunction nanocomposites for photocatalysis: why does face-to-face interface matter?, Frontiers in Materials, 4 (2017) 11.

[3] S. Chu, Y. Cui, N. Liu, The path towards sustainable energy, Nature materials, 16 (2017) 16.

[4] I. Roger, M.A. Shipman, M.D. Symes, Earth-abundant catalysts for electrochemical and photoelectrochemical water splitting, Nature Reviews Chemistry, 1 (2017) 0003.

[5] B. Dou, H. Zhang, G. Cui, Z. Wang, B. Jiang, K. Wang, H. Chen, Y. Xu, Hydrogen production by sorption-enhanced chemical looping steam reforming of ethanol in an alternating fixed-bed reactor: Sorbent to catalyst ratio dependencies, Energy Conversion and Management, 155 (2018) 243-252.

[6] A. Arregi, M. Amutio, G. Lopez, J. Bilbao, M. Olazar, Evaluation of thermochemical routes for hydrogen production from biomass: A review, Energy Conversion and Management, 165 (2018) 696-719.

[7] P. Ganguly, A. Breen, S.C. Pillai, Toxicity of Nanomaterials: Exposure, Pathways, Assessment, and Recent Advances, ACS Biomaterials Science & Engineering, 4 (2018) 2237-2275.

[8] P. Suyana, P. Ganguly, B.N. Nair, A.P. Mohamed, K. Warrier, U. Hareesh, Co 3 O 4–C 3 N 4 p–n nano-heterojunctions for the simultaneous degradation of a mixture of pollutants under solar irradiation, Environmental Science: Nano, 4 (2017) 212-221.

[9] A.E. Burakov, E.V. Galunin, I.V. Burakova, A.E. Kucherova, S. Agarwal, A.G. Tkachev, V.K. Gupta, Adsorption of heavy metals on conventional and nanostructured materials for wastewater treatment purposes: A review, Ecotoxicology and environmental safety, 148 (2018) 702-712.

[10] E.C. Lima, Removal of emerging contaminants from the environment by adsorption, Ecotoxicology and environmental safety, 150 (2018) 1-17.

[11] O.M. Rodriguez-Narvaez, J.M. Peralta-Hernandez, A. Goonetilleke, E.R. Bandala, Treatment technologies for emerging contaminants in water: A review, Chemical Engineering Journal, 323 (2017) 361-380.

[12] Y. Yang, G. Liu, J.T. Irvine, H.M. Cheng, Enhanced photocatalytic H2 production in core–shell engineered rutile TiO2, Advanced Materials, 28 (2016) 5850-5856.

[13] M.N. Huda, Y. Yan, S.-H. Wei, M.M. Al-Jassim, Electronic structure of ZnO: GaN compounds: Asymmetric bandgap engineering, Physical Review B, 78 (2008) 195204.

[14] B. Zhou, J. Song, C. Xie, C. Chen, Q. Qian, B. Han, Mo–Bi–Cd Ternary Metal Chalcogenides: Highly Efficient Photocatalyst for CO2 Reduction to Formic Acid Under Visible Light, ACS Sustainable Chemistry & Engineering, 6 (2018) 5754-5759.

[15] P.K. Santra, P.V. Kamat, Tandem-layered quantum dot solar cells: tuning the photovoltaic response with luminescent ternary cadmium chalcogenides, Journal of the American Chemical Society, 135 (2013) 877-885.

[16] R. Xie, M. Rutherford, X. Peng, Formation of high-quality I− III− VI semiconductor nanocrystals by tuning relative reactivity of cationic precursors, Journal of the American Chemical Society, 131 (2009) 5691-5697.

[17] X. Tang, W.B.A. Ho, J.M. Xue, Synthesis of Zn-doped AgInS2 nanocrystals and their fluorescence properties, The Journal of Physical Chemistry C, 116 (2012) 9769-9773.

[18] B. Chen, N. Pradhan, H. Zhong, From Large-Scale Synthesis to Lighting Device Applications of Ternary I–III–VI Semiconductor Nanocrystals: Inspiring Greener Material Emitters, The journal of physical chemistry letters, 9 (2018) 435-445.

[19] J. Zhong, W. Xiang, C. Xie, X. Liang, X. Xu, Synthesis of spheroidal AgBiS2 microcrystals by L-cysteine assisted method, Materials Chemistry and Physics, 138 (2013) 773-779.

[20] L.T. Bryndzia, O. Kleppa, Standard enthalpies of formation of sulfides and sulfosalts in the Ag-Bi-S system by high-temperature, direct synthesis calorimetry, Economic Geology, 83 (1988) 174-181.
[21] J. Wang, X. Yang, W. Hu, B. Li, J. Yan, J. Hu, Synthesis of AgBiS 2 microspheres by a templating method and their catalytic polymerization of alkylsilanes, Chemical Communications, (2007) 4931-4933.
[22] T. Thongtem, J. Jaroenchaichana, S. Thongtem, Cyclic microwave-assisted synthesis of flower-like and hexapod silver bismuth sulfide, Materials Letters, 63 (2009) 2163-2166.
[23] B. Pejova, I. Grozdanov, D. Nesheva, A. Petrova, Size-dependent properties of sonochemically synthesized three-dimensional arrays of close-packed semiconducting AgBiS2 quantum dots, Chemistry of Materials, 20 (2008) 2551-2565.
[24] H. Liu, J. Zhong, X. Liang, J. Zhang, W. Xiang, A mild biomolecule-assisted route for preparation of flower-like AgBiS2 crystals, Journal of Alloys and Compounds, 509 (2011) L267-L272.
[25] B. Bellal, M. Berger, M. Trari, Physical and photoelectrochemical properties of spherical nanoparticles of α-AgBiS2, Journal of Solid State Chemistry, 254 (2017) 178-183.
[26] J. Han, Z. Liu, K. Guo, J. Ya, Y. Zhao, X. Zhang, T. Hong, J. Liu, High-efficiency AgInS2-modified ZnO nanotube array photoelectrodes for all-solid-state hybrid solar cells, ACS applied materials & interfaces, 6 (2014) 17119-17125.
[27] B. Liu, X. Li, Q. Zhao, J. Ke, M. Tadé, S. Liu, Preparation of AgInS2/TiO2 composites for enhanced photocatalytic degradation of gaseous o-dichlorobenzene under visible light, Applied Catalysis B: Environmental, 185 (2016) 1-10.
[28] Z. Li, B. Wang, Z. Deng, X. Fu, Photoreduction Obtained MoS2/CQDs for Assembly of Ternary MoS2/CQDs/ZnIn2S4 Nanocomposite for Efficient Photocatalytic Hydrogen Evolution under Visible Light, Journal of Materials Chemistry A, (2018).
[29] S. Banerjee, S.C. Pillai, P. Falaras, K.E. O'shea, J.A. Byrne, D.D. Dionysiou, New insights into the mechanism of visible light photocatalysis, The journal of physical chemistry letters, 5 (2014) 2543-2554.
[30] P. Ganguly, C. Byrne, A. Breen, S.C. Pillai, Antimicrobial activity of photocatalysts: fundamentals, mechanisms, kinetics and recent advances, Applied Catalysis B: Environmental, (2017).
[31] J. Mac Mahon, S.C. Pillai, J.M. Kelly, L.W. Gill, Solar photocatalytic disinfection of E. coli and bacteriophages MS2, ΦX174 and PR772 using TiO 2, ZnO and ruthenium based complexes in a continuous flow system, Journal of Photochemistry and Photobiology B: Biology, 170 (2017) 79-90.
[32] V. Etacheri, G. Michlits, M.K. Seery, S.J. Hinder, S.C. Pillai, A highly efficient TiO2–x C x nano-heterojunction photocatalyst for visible light induced antibacterial applications, ACS applied materials & interfaces, 5 (2013) 1663-1672.
[33] S. Panneri, P. Ganguly, B.N. Nair, A.A.P. Mohamed, K.G. Warrier, U.N. Hareesh, Copyrolysed C3N4-Ag/ZnO Ternary Heterostructure Systems for Enhanced Adsorption and Photocatalytic Degradation of Tetracycline, European Journal of Inorganic Chemistry, 2016 (2016) 5068-5076.
[34] S. Zhou, J. Yang, W. Li, Q. Jiang, Y. Luo, D. Zhang, Z. Zhou, X. Li, Preparation and Photovoltaic Properties of Ternary AgBiS2 Quantum Dots Sensitized TiO2 Nanorods Photoanodes by Electrochemical Atomic Layer Deposition, Journal of The Electrochemical Society, 163 (2016) D63-D67.
[35] V. Blum, R. Gehrke, F. Hanke, P. Havu, V. Havu, X. Ren, K. Reuter, M. Scheffler, Ab initio molecular simulations with numeric atom-centered orbitals, Computer Physics Communications, 180 (2009) 2175-2196.
[36] J.P. Perdew, M. Ernzerhof, K. Burke, Rationale for mixing exact exchange with density functional approximations, The Journal of chemical physics, 105 (1996) 9982-9985.
[37] A. Tkatchenko, M. Scheffler, Accurate molecular van der Waals interactions from ground-state electron density and free-atom reference data, Physical review letters, 102 (2009) 073005.
[38] J.D. Head, M.C. Zerner, A Broyden—Fletcher—Goldfarb—Shanno optimization procedure for molecular geometries, Chemical physics letters, 122 (1985) 264-270.

[39] D.J. Griffiths, D.F. Schroeter, Introduction to quantum mechanics, Cambridge University Press2018.
[40] A. Jain, S.P. Ong, G. Hautier, W. Chen, W.D. Richards, S. Dacek, S. Cholia, D. Gunter, D. Skinner, G. Ceder, Commentary: The Materials Project: A materials genome approach to accelerating materials innovation, Apl Materials, 1 (2013) 011002.
[41] S. Panneri, P. Ganguly, M. Mohan, B.N. Nair, A.A.P. Mohamed, K.G. Warrier, U. Hareesh, Photoregenerable, Bifunctional Granules of Carbon-Doped g-C3N4 as Adsorptive Photocatalyst for the Efficient Removal of Tetracycline Antibiotic, ACS Sustainable Chemistry & Engineering, 5 (2017) 1610-1618.
[42] W. Wang, G. Li, D. Xia, T. An, H. Zhao, P.K. Wong, Photocatalytic nanomaterials for solar-driven bacterial inactivation: recent progress and challenges, Environmental Science: Nano, 4 (2017) 782-799.
[43] W. Wang, T.W. Ng, W.K. Ho, J. Huang, S. Liang, T. An, G. Li, C.Y. Jimmy, P.K. Wong, CdIn2S4 microsphere as an efficient visible-light-driven photocatalyst for bacterial inactivation: Synthesis, characterizations and photocatalytic inactivation mechanisms, Applied Catalysis B: Environmental, 129 (2013) 482-490.
[44] P.-C. Huang, W.-C. Yang, M.-W. Lee, AgBiS2 semiconductor-sensitized solar cells, The Journal of Physical Chemistry C, 117 (2013) 18308-18314.
[45] V. Etacheri, M.K. Seery, S.J. Hinder, S.C. Pillai, Highly visible light active TiO2− x N x heterojunction photocatalysts, Chemistry of Materials, 22 (2010) 3843-3853.
[46] H.-B. Yao, M.-R. Gao, S.-H. Yu, Small organic molecule templating synthesis of organic–inorganic hybrid materials: their nanostructures and properties, Nanoscale, 2 (2010) 322-334.
[47] N. Jiang, R. Wu, J. Li, Y. Sun, J. Jian, Ethanol amine-assisted solvothermal growth of wurtzite-structured ZnS thin nanorods, Journal of Alloys and Compounds, 536 (2012) 85-90.
[48] Z. Chen, X. Qin, T. Zhou, X. Wu, S. Shao, M. Xie, Z. Cui, Ethanolamine-assisted synthesis of size-controlled indium tin oxide nanoinks for low temperature solution deposited transparent conductive films, Journal of Materials Chemistry C, 3 (2015) 11464-11470.
[49] X. Wang, Q. Zhang, Q. Wan, G. Dai, C. Zhou, B. Zou, Controllable ZnO architectures by ethanolamine-assisted hydrothermal reaction for enhanced photocatalytic activity, The Journal of Physical Chemistry C, 115 (2011) 2769-2775.
[50] J. Hu, B. Deng, K. Tang, C. Wang, Y. Qian, Preparation and phase control of nanocrystalline silver indium sulfides via a hydrothermal route, Journal of Materials Research, 16 (2001) 3411-3415.
[51] N. Tipcompor, S. Thongtem, T. Thongtem, Transformation of cubic AgBiS2 from nanoparticles to nanostructured flowers by a microwave-refluxing method, Ceramics International, 39 (2013) S383-S387.
[52] I. Martina, R. Wiesinger, D. Jembrih-Simbürger, M. Schreiner, Micro-Raman characterisation of silver corrosion products: instrumental set up and reference database, E-Preservation Science: Morana RTD [Online], (2012) 1-8.
[53] S.N. Guin, S. Banerjee, D. Sanyal, S.K. Pati, K. Biswas, Origin of the Order–Disorder Transition and the Associated Anomalous Change of Thermopower in AgBiS2 Nanocrystals: A Combined Experimental and Theoretical Study, Inorganic chemistry, 55 (2016) 6323-6331.
[54] C. Byrne, R. Fagan, S. Hinder, D.E. McCormack, S.C. Pillai, New approach of modifying the anatase to rutile transition temperature in TiO 2 photocatalysts, RSC Advances, 6 (2016) 95232-95238.
[55] S. Mathew, P. Ganguly, S. Rhatigan, V. Kumaravel, C. Byrne, S. Hinder, J. Bartlett, M. Nolan, S. Pillai, Cu-Doped TiO2: Visible Light Assisted Photocatalytic Antimicrobial Activity, Applied Sciences, 8 (2018) 2067.
[56] Y. Zhu, Y. Wang, Q. Ling, Y. Zhu, Enhancement of full-spectrum photocatalytic activity over BiPO 4/Bi 2 WO 6 composites, Applied Catalysis B: Environmental, 200 (2017) 222-229.

[57] N. Li, T. Lv, Y. Yao, H. Li, K. Liu, T. Chen, Compact graphene/MoS 2 composite films for highly flexible and stretchable all-solid-state supercapacitors, Journal of Materials Chemistry A, 5 (2017) 3267-3273.

[58] V. Etacheri, M.K. Seery, S.J. Hinder, S.C. Pillai, Oxygen rich titania: A dopant free, high temperature stable, and visible-light active anatase photocatalyst, Advanced Functional Materials, 21 (2011) 3744-3752.

[59] N.S. Leyland, J. Podporska-Carroll, J. Browne, S.J. Hinder, B. Quilty, S.C. Pillai, Highly Efficient F, Cu doped TiO2 anti-bacterial visible light active photocatalytic coatings to combat hospital-acquired infections, Scientific reports, 6 (2016).

[60] D. Liu, D. Cai, Y. Yang, H. Zhong, Y. Zhao, Y. Song, S. Yang, H. Wu, Solvothermal synthesis of carbon nanotube-AgBiS2 hybrids and their optical limiting properties, Applied Surface Science, 366 (2016) 30-37.

[61] M.-H. Sun, S.-Z. Huang, L.-H. Chen, Y. Li, X.-Y. Yang, Z.-Y. Yuan, B.-L. Su, Applications of hierarchically structured porous materials from energy storage and conversion, catalysis, photocatalysis, adsorption, separation, and sensing to biomedicine, Chemical Society Reviews, 45 (2016) 3479-3563.

[62] R. Nyholm, A. Berndtsson, N. Martensson, Core level binding energies for the elements Hf to Bi (Z= 72-83), Journal of Physics C: Solid State Physics, 13 (1980) L1091.

[63] G. Muilenberg, Handbook of X-ray photoelectron spectroscopy, Perkin-Elmer Corporation, (1979) 64.

[64] Z. Zhang, K. Liu, Z. Feng, Y. Bao, B. Dong, Hierarchical sheet-on-sheet ZnIn 2 S 4/gC 3 N 4 heterostructure with highly efficient photocatalytic H 2 production based on photoinduced interfacial charge transfer, Scientific reports, 6 (2016) 19221.

[65] G. Yang, D. Chen, H. Ding, J. Feng, J.Z. Zhang, Y. Zhu, S. Hamid, D.W. Bahnemann, Well-designed 3D ZnIn2S4 nanosheets/TiO2 nanobelts as direct Z-scheme photocatalysts for CO2 photoreduction into renewable hydrocarbon fuel with high efficiency, Applied Catalysis B: Environmental, 219 (2017) 611-618.

[66] Y. Xia, Q. Li, K. Lv, D. Tang, M. Li, Superiority of graphene over carbon analogs for enhanced photocatalytic H2-production activity of ZnIn2S4, Applied Catalysis B: Environmental, 206 (2017) 344-352.

[67] G. Yang, H. Ding, D. Chen, J. Feng, Q. Hao, Y. Zhu, Construction of urchin-like ZnIn2S4-Au-TiO2 heterostructure with enhanced activity for photocatalytic hydrogen evolution, Applied Catalysis B: Environmental, 234 (2018) 260-267.

[68] S.M. Sze, K.K. Ng, Physics of semiconductor devices, John wiley & sons2006.

[69] N. Serpone, D. Lawless, R. Khairutdinov, Size effects on the photophysical properties of colloidal anatase TiO2 particles: size quantization versus direct transitions in this indirect semiconductor?, The journal of Physical Chemistry, 99 (1995) 16646-16654.

[70] E. Davis, N. Mott, Conduction in non-crystalline systems V. Conductivity, optical absorption and photoconductivity in amorphous semiconductors, Philosophical Magazine, 22 (1970) 0903-0922.

[71] E. Yablonovitch, Photonic band-gap structures, JOSA B, 10 (1993) 283-295.

[72] S. Kaowphong, Biomolecule-assisted hydrothermal synthesis of silver bismuth sulfide with nanostructures, Journal of Solid State Chemistry, 189 (2012) 108-111.

[73] C. Han, R. Luque, D.D. Dionysiou, Facile preparation of controllable size monodisperse anatase titania nanoparticles, Chemical Communications, 48 (2012) 1860-1862.

[74] M. Deng, S. Shen, Y. Zhang, H. Xu, Q. Wang, A generalized strategy for controlled synthesis of ternary metal sulfide nanocrystals, New Journal of Chemistry, 38 (2014) 77-83.

[75] S. Panneri, P. Ganguly, B.N. Nair, A.A.P. Mohamed, K.G.K. Warrier, U.N.S. Hareesh, Role of precursors on the photophysical properties of carbon nitride and its application for antibiotic degradation, Environmental Science and Pollution Research, 24 (2017) 8609-8618.

[76] W. Wang, L. Zhang, T. An, G. Li, H.-Y. Yip, P.-K. Wong, Comparative study of visible-light-driven photocatalytic mechanisms of dye decolorization and bacterial disinfection by B–Ni-codoped TiO2

microspheres: The role of different reactive species, Applied Catalysis B: Environmental, 108 (2011) 108-116.
[77] X.-D. Zhu, Y.-J. Wang, R.-J. Sun, D.-M. Zhou, Photocatalytic degradation of tetracycline in aqueous solution by nanosized TiO2, Chemosphere, 92 (2013) 925-932.
[78] A.A. Borghi, M.S.A. Palma, Tetracycline: production, waste treatment and environmental impact assessment, Brazilian Journal of Pharmaceutical Sciences, 50 (2014) 25-40.
[79] J. Bolobajev, M. Trapido, A. Goi, Effect of iron ion on doxycycline photocatalytic and Fenton-based autocatatalytic decomposition, Chemosphere, 153 (2016) 220-226.
[80] T. Verdier, M. Coutand, A. Bertron, C. Roques, Antibacterial activity of TiO2 photocatalyst alone or in coatings on E. coli: the influence of methodological aspects, Coatings, 4 (2014) 670-686.
[81] K.E. Karakitsou, X.E. Verykios, Effects of altervalent cation doping of titania on its performance as a photocatalyst for water cleavage, The Journal of Physical Chemistry, 97 (1993) 1184-1189.
[82] Y. Yang, X.-j. Li, J.-t. Chen, L.-y. Wang, Effect of doping mode on the photocatalytic activities of Mo/TiO2, Journal of Photochemistry and Photobiology A: Chemistry, 163 (2004) 517-522.
[83] R. Kumar, A. Umar, G. Kumar, M. Akhtar, Y. Wang, S. Kim, Ce-doped ZnO nanoparticles for efficient photocatalytic degradation of direct red-23 dye, Ceramics International, 41 (2015) 7773-7782.
[84] M. Mousavi, A. Habibi-Yangjeh, M. Abitorabi, Fabrication of novel magnetically separable nanocomposites using graphitic carbon nitride, silver phosphate and silver chloride and their applications in photocatalytic removal of different pollutants using visible-light irradiation, Journal of colloid and interface science, 480 (2016) 218-231.
[85] R.S. Mulliken, A new electroaffinity scale; together with data on valence states and on valence ionization potentials and electron affinities, The Journal of Chemical Physics, 2 (1934) 782-793.
[86] A. Habibi-Yangjeh, M. Shekofteh-Gohari, Novel magnetic Fe3O4/ZnO/NiWO4 nanocomposites: Enhanced visible-light photocatalytic performance through pn heterojunctions, Separation and Purification Technology, 184 (2017) 334-346.
[87] R. Bose, G. Manna, S. Jana, N. Pradhan, Ag2S–AgInS2: p–n junction heteronanostructures with quasi type-II band alignment, Chemical Communications, 50 (2014) 3074-3077.